# Supporting Information

## Realizing Horizontal Magnesium Platelet Deposition and Suppressed Surface Passivation for High-Performance Magnesium Metal Batteries

*Gaoliang Yang,[a] Yuanjian Li,[a] Jianbiao Wang,[a] Yanwei Lum,[a] Carina Yi Jing Lim,[a] Man-Fai Ng,[b] Chang Zhang,[c] Zhi Chang,[d] Zhonghan Zhang,[e] Albertus D. Handoko,[a] Tanmay Ghosh,[a] Shuzhou Li,[e] Zdenek Sofer,[f] Wei Liu,[c] Yan Yao,*[gh] and Zhi Wei Seh*[a]*

*a. Institute of Materials Research and Engineering (IMRE), Agency for Science, Technology and Research (A*STAR) , 2 Fusionopolis Way, Innovis #08-03, Singapore 138634, Republic of Singapore*

*b. Institute of High Performance Computing (IHPC), Agency for Science, Technology and Research (A*STAR), 1 Fusionopolis Way, #16-16 Connexis, Singapore 138632, Republic of Singapore*

*c. School of Physical Science and Technology, ShanghaiTech University, Shanghai 201210, China*

*d. Department of Materials Physics and Chemistry, School of Materials Science & Engineering, Central South University, Changsha, 410083, Hunan, China*

*e. School of Materials Science and Engineering, Nanyang Technological University, 50 Nanyang Ave, Singapore 639798, Republic of Singapore*

*f. Department of Inorganic Chemistry, University of Chemistry and Technology Prague, Technická 5, 166 28 Prague 6, Czech Republic*

*g. Department of Electrical and Computer Engineering, University of Houston, Houston, TX 77204, USA*

*h. Texas Center for Superconductivity at the University of Houston (TcSUH), University of Houston, Houston, TX 77204, USA*

**Author to whom correspondence should be addressed.*

*Email: yyao4@uh.edu; sehzw@imre.a-star.edu.sg*

**Experimental Section**

*Electrolyte preparation:* Firstly, 1,2-dimethoxyethane (DME, 99.5%, anhydrous, Sigma-Aldrich) was dried with molecular sieves (3Å beads, 4-8 mesh, Sigma-Aldrich) in advance. 0.2 M magnesium triflate ($Mg(OTf)_2$, 99.5%, Solvionic) was then added into the DME solvent, stirring at 50 ℃ in the glovebox until the solution became clear. Finally, the above pure $Mg(OTf)_2$ electrolyte was modified with different amounts of 1-chloropropane (CP, 98%, Sigma-Aldrich). All of the prepared electrolytes were added with molecular sieves to remove any remaining moisture in the solution.

*Materials characterization:* In our investigation, the morphology was studied using scanning electron microscopy (SEM) (JEOL 7600F), coupled with energy dispersive X-ray spectrometer (EDS) to determine elementary composition. The cross-sectional view of the cycled electrodes was characterized by focused-ion-beam assisted scanning electron microscopy (FIB-SEM, Helios NanoLab 450S, 30 KeV and 2.5 nA for cutting). X-ray diffraction (XRD) patterns were measured on an X-ray diffractometer (D8 Advance, Bruker) with Cu-Kα radiation under 40 kV and 40 mA. The chemical compositions of samples were characterized by X-ray photoelectron spectroscopy (XPS) (Thermo Fisher Scientific, with Al Kα radiation of 1486.6 eV) and time-of-flight secondary ion mass spectrometry (TOF-SIMS) (IONTOF GmbH, Germany measurements). The area for TOF-SIMS measurement is 100 μm × 100 μm, and the etching depth is ~0.8 μm. Wide-angle X-ray scattering (WAXS) patterns were measured using Bruker D8 Discover goniometer equipped with a capillary focused IμS 2.0 Cu Ka X-ray source (50 kV, 1000 μA). The structure of electrolytes was characterized using Raman spectroscopy (Renishaw 200 system with a 532-nm excitation laser). For the characterization of electrodes, all the electrodes were disassembled from the coin cells in an Ar-filled glove box ($H_2O$ < 0.1 ppm and $O_2$ < 1 ppm). The electrodes were washed with DME solvent and dried at room temperature for further analysis. Airtight sample holders were used to transfer samples from the glovebox to the sample chamber.

*Cryogenic transmission electron microscopy (cryo-TEM) sample preparation and characterization:* After deposition, the TEM grid was disassembled from the coin cell in an Ar-filled glove box ($H_2O$ < 0.1 ppm and $O_2$ < 1 ppm). The grid was slightly rinsed with DME solvent to remove trace electrolyte. After drying, the sample was transferred into cryo-TEM holder (Gatan) in the glovebox, and closed the shuttle on the holder. The cryo-TEM holder was protected by an Ar protection sealed container, and quickly inserted into TEM (FEI, Titan), and then liquid nitrogen was poured into the cryo-TEM holder to cool the sample temperature to -170 °C. The cryo-TEM testing was taken at cryogenic temperature of -170°C.

*Electrochemical measurements:* The electrochemical performance was evaluated using 2032-type coin cells on Neware Battery Tester. For the assembling of asymmetric cells, a carbon-coated Al disk (1 $cm^2$) (MTI) was utilized as the working electrode, a polished Mg disk (1.26 $cm^2$) (99.9%, 0.1 mm thick, MTI) was used as the counter electrode, and a layer of glass fiber (Whatman GF/A) as the separator. The cell was filled with 75 μL of electrolyte solution. In the symmetric cell configuration, the Al disk was replaced with polished Mg disks (1.26 $cm^2$). All the other components in the coin cell were washed with ethanol and dried at 60 ℃ overnight. Electrochemical impedance spectroscopy (EIS) was carried out on symmetric cells using Gamry Potentiostat between 100 kHz to 0.1 Hz. The Coulombic efficiency (CE) of the Mg plating and stripping process was evaluated by conducting galvanostatic cycling in the Mg//Al asymmetric cells (coin cell 2032). In each test cycle (taking 0.5 mA $cm^{-2}$/0.5 mAh $cm^{-2}$ condition as example), different areal capacities of magnesium are plated on the working electrode by applying a current density of 0.5 mA $cm^{-2}$ to the electrode for 1 hour. Subsequently, the same current is applied to strip Mg from the electrode until the potential of the working electrode reached the cut-off potential of 1.2 V. The CE of the cell is calculated by the formula:

$$CE = \frac{magnesium\ dissolution\ capacity}{magnesium\ deposition\ capacity} \times 100\%$$

For the fabrication of Mg//$Mo_6S_8$ cells, the $Mo_6S_8$ with Chevrel phase was prepared according to our previous work.[1] Then the cathode slurry was prepared by mixing $Mo_6S_8$, Super P carbon black, and polyvinylidene difluoride (PVDF) binder in the weight ratio of 80:10:10 in *N*-methyl-2-pyrrolidone (NMP) solvent. The slurry was coated on Ni foil and dried in the vacuum oven at 60 ℃ for 12 h. The electrodes were punched into 12-mm-diameter disks, the areal mass loading on which was controlled to be ~ 2 mg $cm^{-2}$.

For the fabrication of Mg//PTCDA (3,4,9,10-perylenetetracarboxylic dianhydride) cells, the PTCDA (97%, Sigma-Aldrich) was mixed with Super P carbon black and PVDF with a mass ratio of 7:2:1. The mixture was then grinded with NMP solvent to form a uniform slurry, and coated uniformly onto a carbon cloth and dried at 60 °C under vacuum for 12 h. The electrodes were punched into 12-mm-diameter disks, the areal mass loading on which was controlled to be ~ 1 mg $cm^{-2}$.

*DFT calculation:* DFT calculations for frontier orbital information were carried out under the level of theory of the B3LYP functional[2] with D3BJ dispersion corrections[3] in conjunction with the 6-311 g(d,p) basis set.[4] Computations of all molecules were performed with geometry optimization, followed by single point energy calculation for accurate adsorption energy and frontier orbital information extraction. The computations were performed with Gaussian 16a software,[5] and molecular orbital information extraction and analysis were performed via Multiwfn.[6]

Geometry optimizations are performed using DFT with the Perdew, Burke, and Ernzerhof (PBE) exchange-correlation functional[7] implemented in Vienna Ab-initio Simulation Package (version 5.4).[8] The projector augmented wave (PAW) method[9] is used to describe the core−valence interactions. Spin-polarization calculations are carried out. The kinetic energy cut off for the plane-wave expansion is set at 600 eV. A 5×5×1 Gamma sampling k-point grid is used for the slabs. The bottom two layers of atoms in the slabs are frozen and the lattices are

kept fixed at the optimized bulk values, and the rest of the ions are fully relaxed during optimizations. The thresholds of the total energy and absolute value of the forces acting on each atom are set at $1\times10^{-6}$ eV and $1\times10^{-2}$ eV Å$^{-1}$, respectively. A vacuum layer of at least 15 Å and dipole corrections are applied for the slabs. The DFT-D3 method[10] is applied to correct the dispersion interactions. The surface energy ($\gamma$) is calculated using the equation: $\gamma = \frac{1}{2A}(E_{slab} - NE_{bulk}^{mg} - N_{ads}E_{ads})$ where $A$ is the area of the slab, $E_{slab}$ is the total energy of the slab, $E_{bulk}^{mg}$ is the energy per unit of Mg, $N$ is the total number of unit Mg in the slab, $E_{ads}$ is the energy per unit of the adsorbent determined from bulk or molecular states, and $N_{ads}$ is the total number of unit adsorbent in the slab. Slabs with adsorbents on both sides are used and all ions are relaxed during optimizations for the surface energy calculations.

*COMSOL simulation:* The Finite Element Analysis method was employed to simulate the dissolution-deposition process and the growth of deposit by COMSOL Multiphysics software. "Tertiary current distribution (Nernst-Planck) interface" and "deforming geometry interface" were coupled to simulate the real-time electrochemical progress. The electrochemical reaction kinetics at the electrode-electrolyte interface could be described by using concentration dependent equation (modified Butler-Volmer equation):

$$i_{loc} = i_0\left(c_R\, exp\left(\frac{\alpha_a F\eta}{RT}\right) - c_O exp\left(\frac{-\alpha_c F\eta}{RT}\right)\right)$$

Where, $i_{loc}$ is the actual exchange current density, $i_0$ represents exchange current density, $c_R$ and $c_O$ are the concentration of reduction and oxidation species respectively, $\alpha_a$ and $\alpha_c$ are the anodic and cathodic charge transfer coefficients, $\eta$ is the overpotential, $T$ is the system temperature, $F$ is the ideal gas constant. The simulation symmetric cells were modeled by using 2D geometry. Here, the top side represents the electrode surface of counter electrode (Mg metal), where the $Mg^{2+}$ dissolves into the electrolyte. The bottom areas with different morphologies refer to the deposited metal electrode, where $Mg^{2+}$ was reduced into Mg metal. The whole system was filled

with various electrolytes (pure $Mg(OTf)_2$, and $Mg(OTf)_2$ + CP). In the modelling deposition process, the potential of bottom electrode is set as 0 V, and the applied average current density is 0.5 mA $cm^{-2}$.

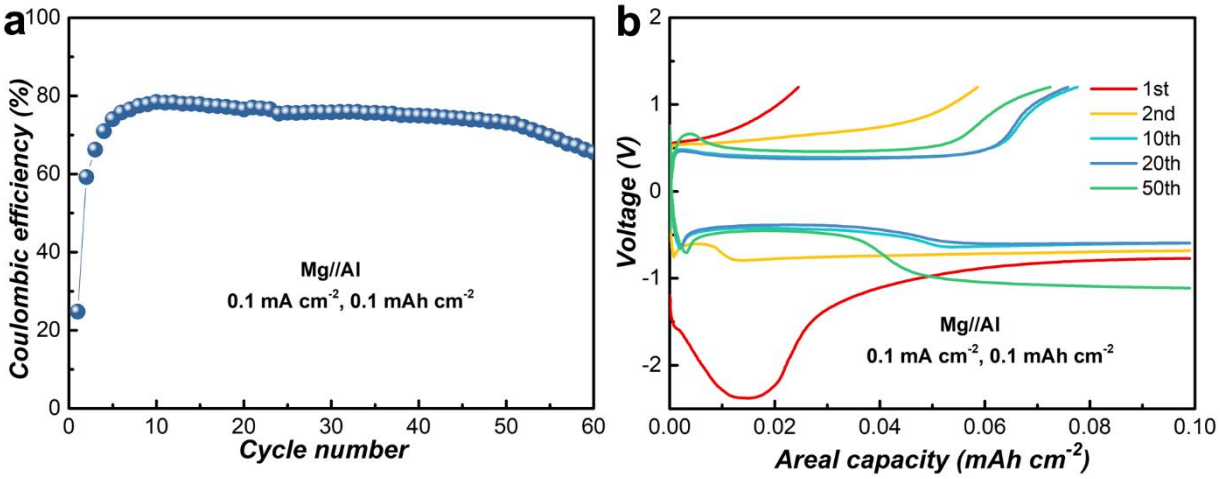


**Figure S1**. Cycling performance of Mg//Al asymmetric cells with pure $Mg(OTf)_2$ electrolyte at 0.1 mA $cm^{-2}$ and 0.1 mAh $cm^{-2}$. a) Coulombic efficiency (CE) versus cycle number and b) voltage profiles from different cycles.

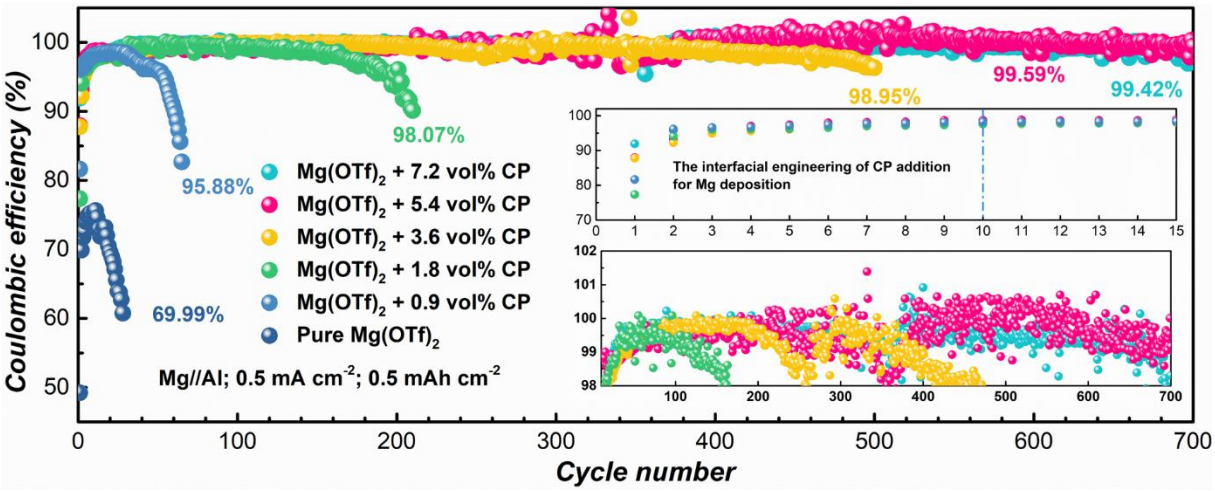


**Figure S2**. CEs of Mg plating/stripping in the asymmetric cells using different electrolytes at 0.5 mA $cm^{-2}$ and 0.5 mAh $cm^{-2}$.The inset is the variations of CEs in the first 15 cycles and the enlarged Y ranges for CEs with different amounts of CP in the electrolytes.

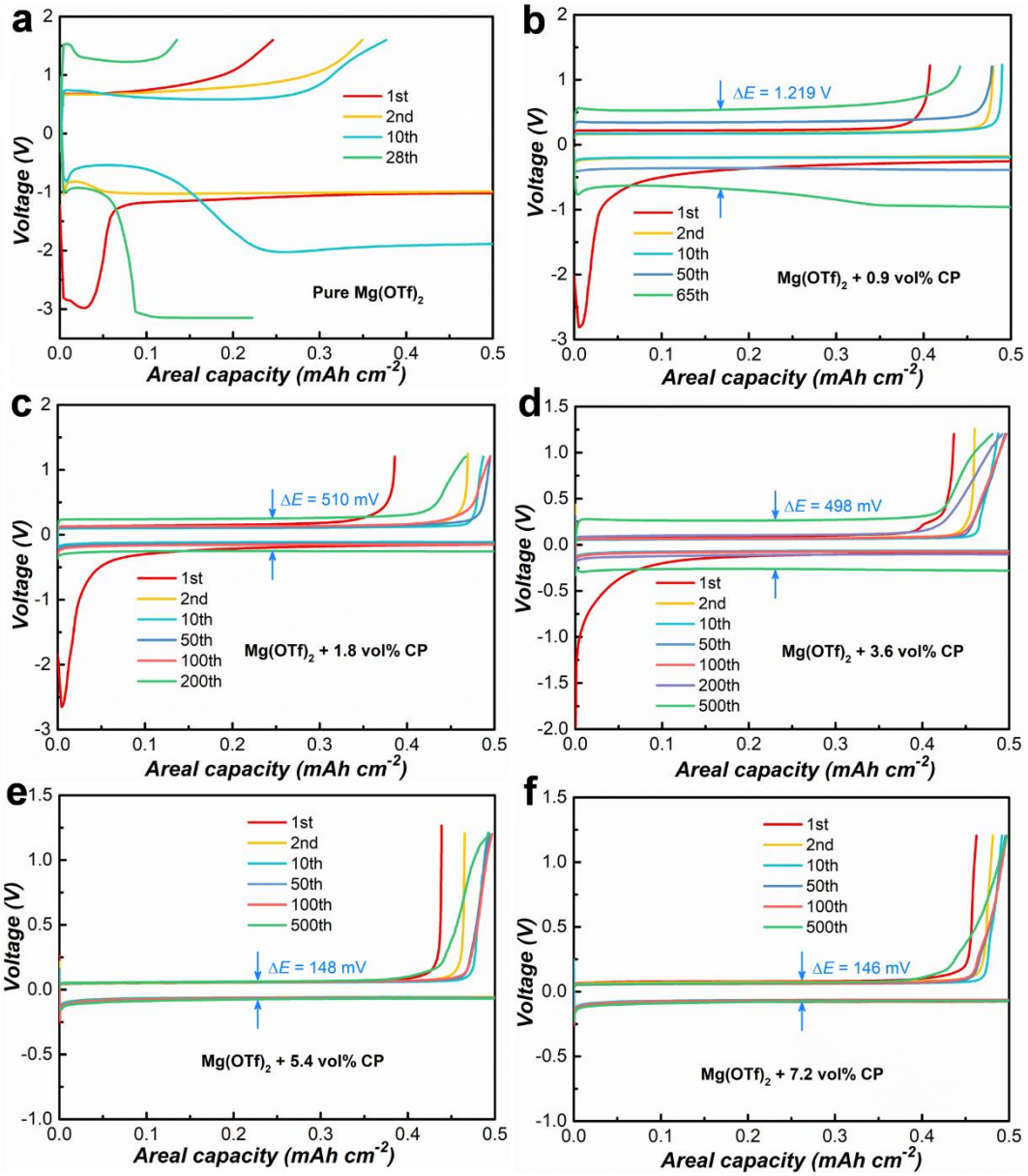


**Figure S3**. Voltage profiles of Mg plating/stripping with Mg//Al asymmetric cells at 0.5 mA $cm^{-2}$ and 0.5 mAh $cm^{-2}$ in different electrolytes of a) pure $Mg(OTf)_2$, b) $Mg(OTf)_2$ + 0.9 vol% CP, c) $Mg(OTf)_2$ + 1.8 vol% CP, d) $Mg(OTf)_2$ + 3.6 vol% CP, e) $Mg(OTf)_2$ + 5.4 vol% CP and f) $Mg(OTf)_2$ + 7.2 vol% CP.

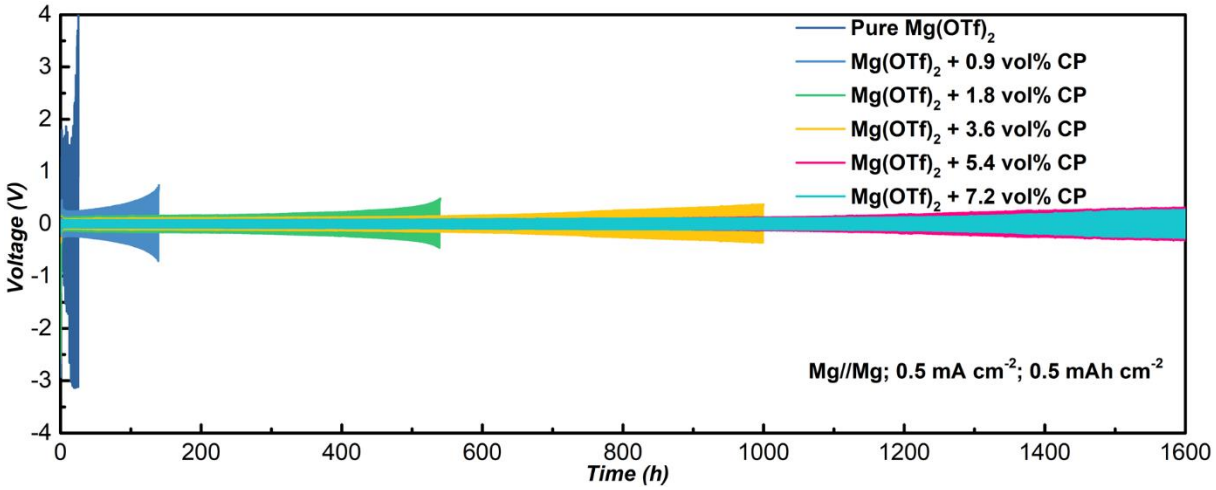


**Figure S4.** Galvanostatic cycling performance of Mg//Mg symmetric cells at 0.5 mA $cm^{-2}$ and 0.5 mAh $cm^{-2}$ with varied amounts of CP in the electrolytes.

Note to Figure S2-S4: A range of electrolytes modified using varying amounts of CP were prepared and the reversibility of Mg plating/stripping with these electrolytes was evaluated using Mg//Al asymmetric cells. Figure S2 depicts the poor performance of pure $Mg(OTf)_2$ electrolyte (0.2 M $Mg(OTf)_2$/1,2-dimethoxyethane (DME)) with CE values averaging at a mere 69.99%, symptomatic of severe passivation from the irreversible consumption of both $Mg^{2+}$ and solvent from the electrolyte. In stark contrast, the addition of 0.9 vol% CP in $Mg(OTf)_2$ electrolyte dramatically enhances the average CE to 95.88%. This improvement is positively correlated with increasing CP amounts, with average CE values increasing from 98.07% to 98.95% with CP amounts from 1.8 vol% to 3.6 vol%, eventually peaking 99.59% at 5.4 vol%. Another key indicator of reversibility is the overpotential associated with the plating/stripping processes, which also decreases with the addition of CP (Figure S3), thereby suggesting a reduction in the interfacial resistances.[11] Owing to the enhanced reversibility and reduced interfacial resistances, the CP modified electrolytes can significantly enhance the cycling stability of Mg anodes (from mere 30 cycles to several hundred cycles). Past 5.4 vol%, further increment in CP amount to 7.2 vol% had negligible effects on the CE and overpotential (Figure S2-S3). Thus, 5.4 vol% is regarded as the optimal amount for CP additive in this work, and 0.2

M $Mg(OTf)_2$ + 5.4 vol% CP is described as $Mg(OTf)_2$ + CP hereinafter. The effects of CP addition for the Mg//Mg symmetric cells were also evaluated at 0.5 mA $cm^{-2}$ and 0.5 mAh $cm^{-2}$ (Figure S4), in consistent with the performance in Mg//Al asymmetric cells, the addition of CP can significantly reduce the overpotential and enhance the cycling duration for the $Mg(OTf)_2$ electrolyte in Mg//Mg symmetric cells.

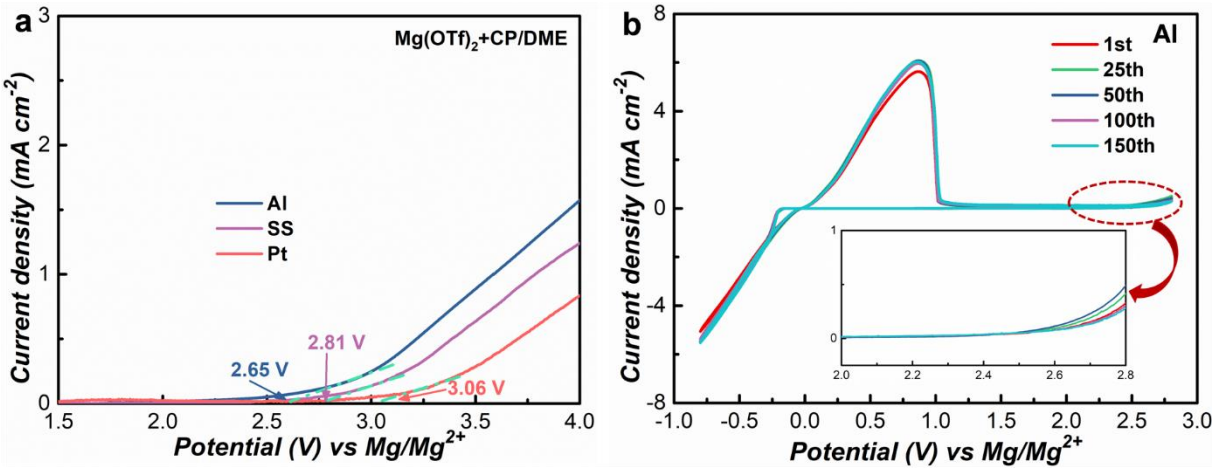


**Figure S5.** a) The LSV curves of $Mg(OTf)_2$ + CP electrolyte on different working electrodes. b) The CV curves of $Mg(OTf)_2$ + CP electrolyte with Al electrode. The scan rate is 5 mV $s^{-1}$.

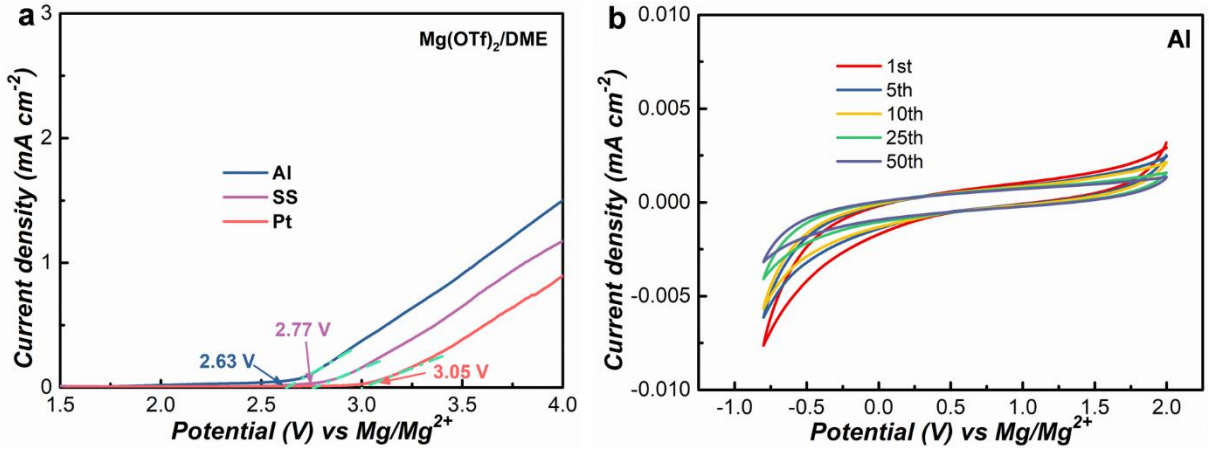


**Figure S6.** a) The LSV curves of pure $Mg(OTf)_2$ electrolyte on different working electrodes. b) The CV curves of pure $Mg(OTf)_2$ electrolyte with Al electrode. The scan rate is 5 mV $s^{-1}$.

Note to Figure S5-S6: To evaluate the oxidation stability of electrolytes, linear sweep voltammetry (LSV) was conducted on different metal electrodes in a three-electrode system. As displayed in Figure S5a, the oxidation potentials of $Mg(OTf)_2$ + CP electrolyte on Al, SS and Pt are 2.65, 2.81 and 3.06 V (versus $Mg/Mg^{2+}$), respectively, which are similar to the measured potentials in pure $Mg(OTf)_2$ electrolyte (Figure S6a). This indicates that the addition of CP has negligible influence on the electrolyte's anodic stability. In addition, Mg plating/stripping behaviours of the electrolytes were investigated by cyclic voltammetry (CV) (the working electrode is Al). No reversible Mg plating/stripping processes were observed in pure $Mg(OTf)_2$ electrolyte (Figure S6b), while highly reversible plating/stripping behaviours were observed in $Mg(OTf)_2$ + CP electrolyte (Figure S5b). The almost overlapping CV curves over different cycles, coupled with the galvanostatic cycling performance of the asymmetric cells, highlights the superior cycling stability of $Mg(OTf)_2$ + CP electrolyte.

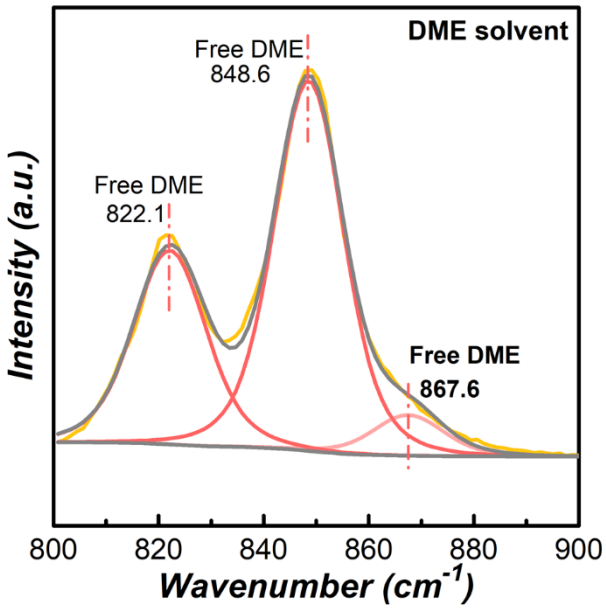


**Figure S7.** Raman spectrum of DME solvent.

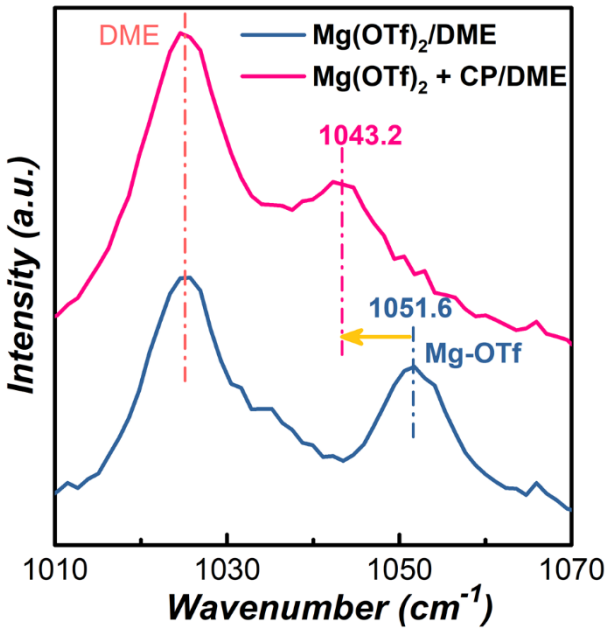


**Figure S8.** Raman spectra of $Mg(OTf)_2$/DME and $Mg(OTf)_2$ + CP/DME electrolytes.

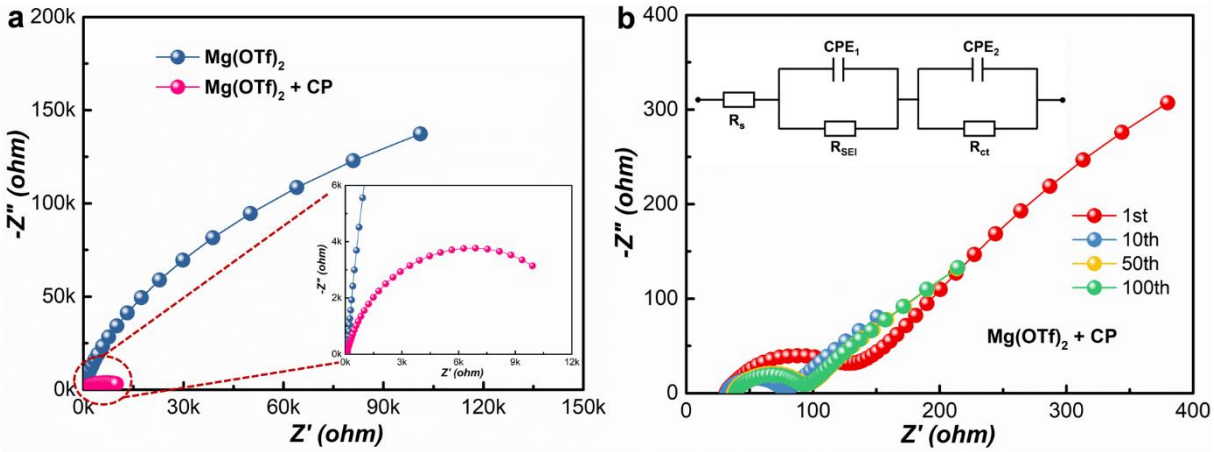


**Figure S9.** a) EIS measurements of Mg//Mg symmetric cell with different electrolytes before cycling. b) Impedance spectra of Mg//Mg cell with $Mg(OTf)_2$ + CP electrolyte after different cycles at 0.5 mA $cm^{-2}$ and 0.5 mAh $cm^{-2}$. The inset in Figure S9b is the corresponding equivalent circuit, in which $R_s$ indicates the bulk resistance of electrolyte, separator, and electrodes; $R_{SEI}$ represents the resistance of ion migration through the SEI; $R_{ct}$ stands for the resistance of charge transfer.

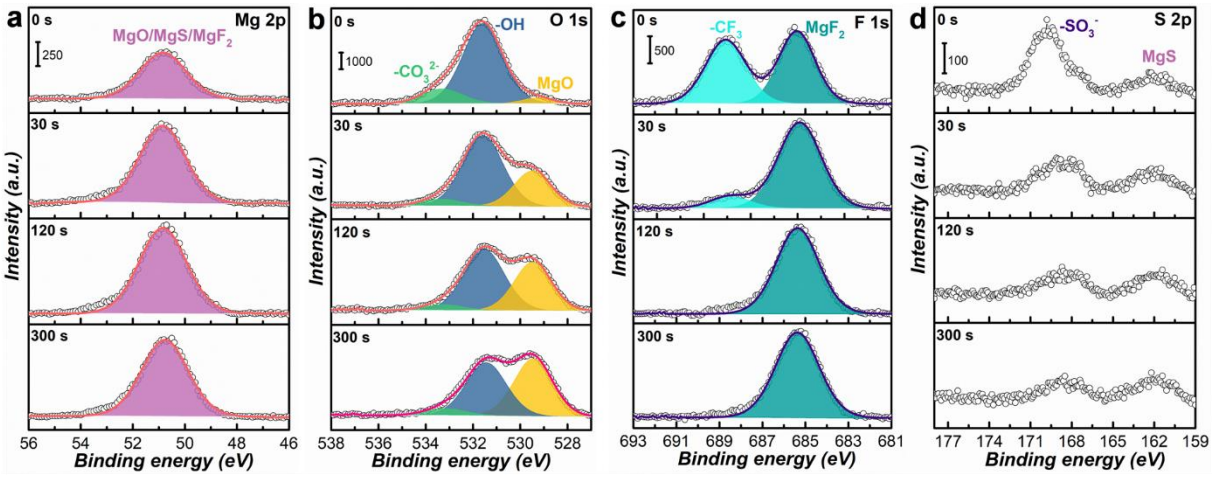


**Figure S10**. XPS spectra of cycled Mg electrode in pure $Mg(OTf)_2$ electrolyte at 0.5 mA $cm^{-2}$ and 0.5 mAh $cm^{-2}$ on the top surface (0 s), after Ar etching for 30 s, 120 s and 300 s. a) Mg 2p, b) O 1s, c) F 1s and d) S 2p.

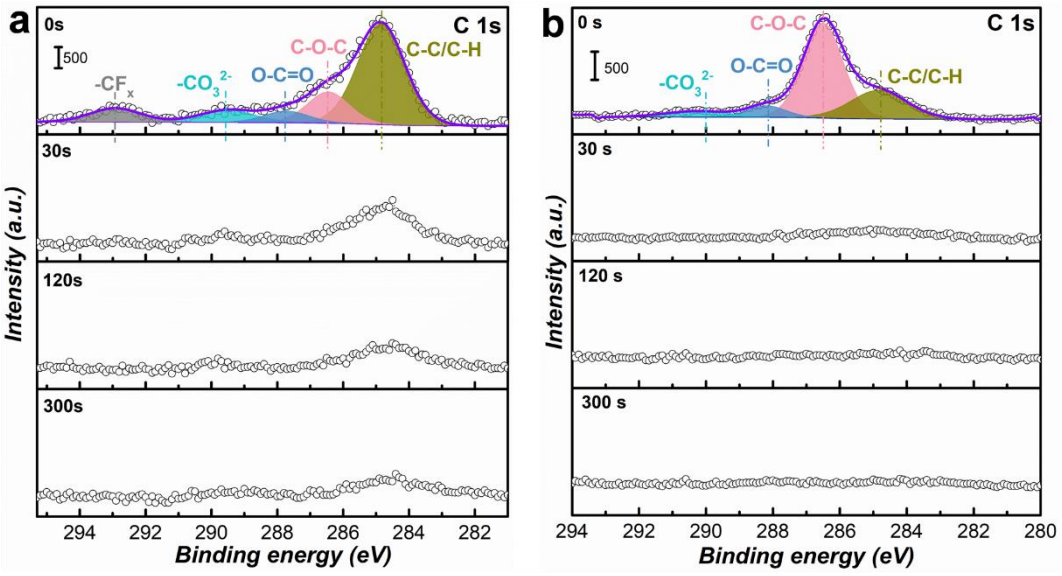


**Figure S11.** The comparison of C 1s XPS depth analysis of cycled Mg electrodes in a) pure $Mg(OTf)_2$ and b) $Mg(OTf)_2$ + CP electrolytes**.**

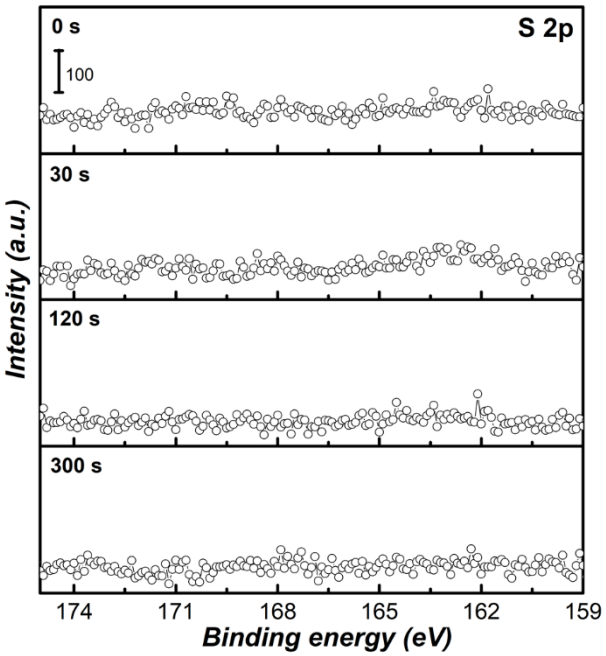


**Figure S12**. S 2p XPS spectra of the cycled Mg electrode in $Mg(OTf)_2$ + CP electrolyte with different Ar etching times.

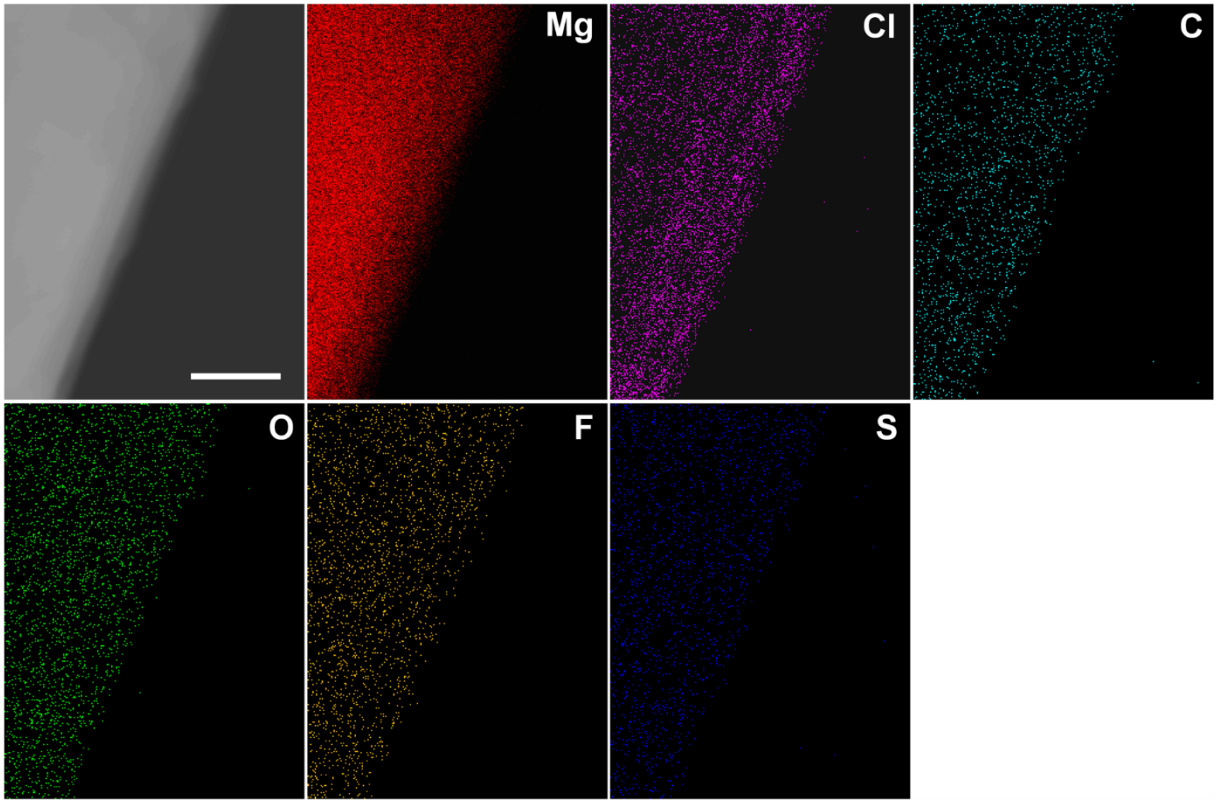


**Figure S13.** EDS elemental mappings of the in-situ formed Cl-rich interphase on Mg deposits with $Mg(OTf)_2$ + CP electrolyte. The scale bar is 10 nm.

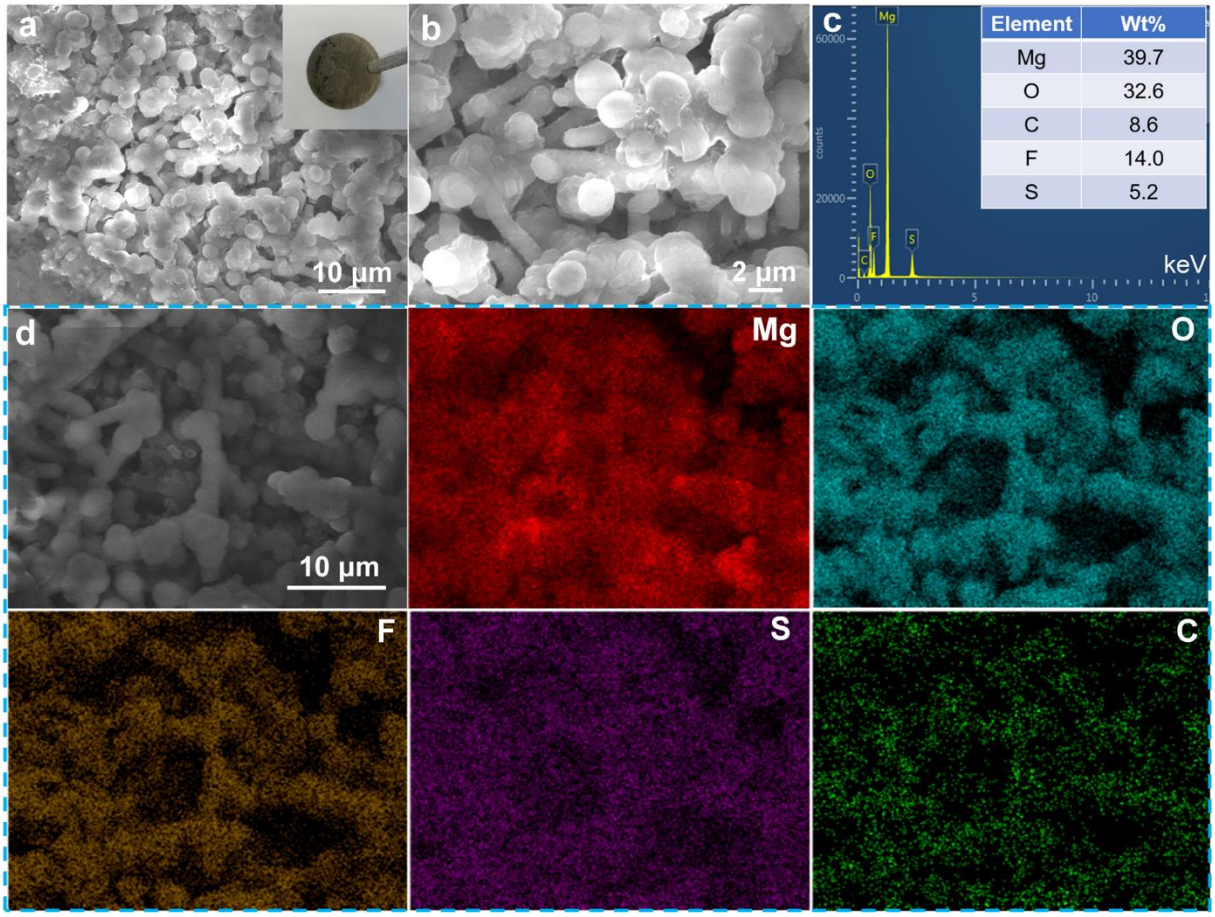


**Figure S14**. a-b) Typical SEM images (inset is the optical image) and the corresponding c) EDS spectrum and d) elemental mapping of the cycled Mg electrode from Mg//Mg symmetric cells in pure $Mg(OTf)_2$ electrolyte at 0.5 mA $cm^{-2}$ and 0.5 mAh $cm^{-2}$.

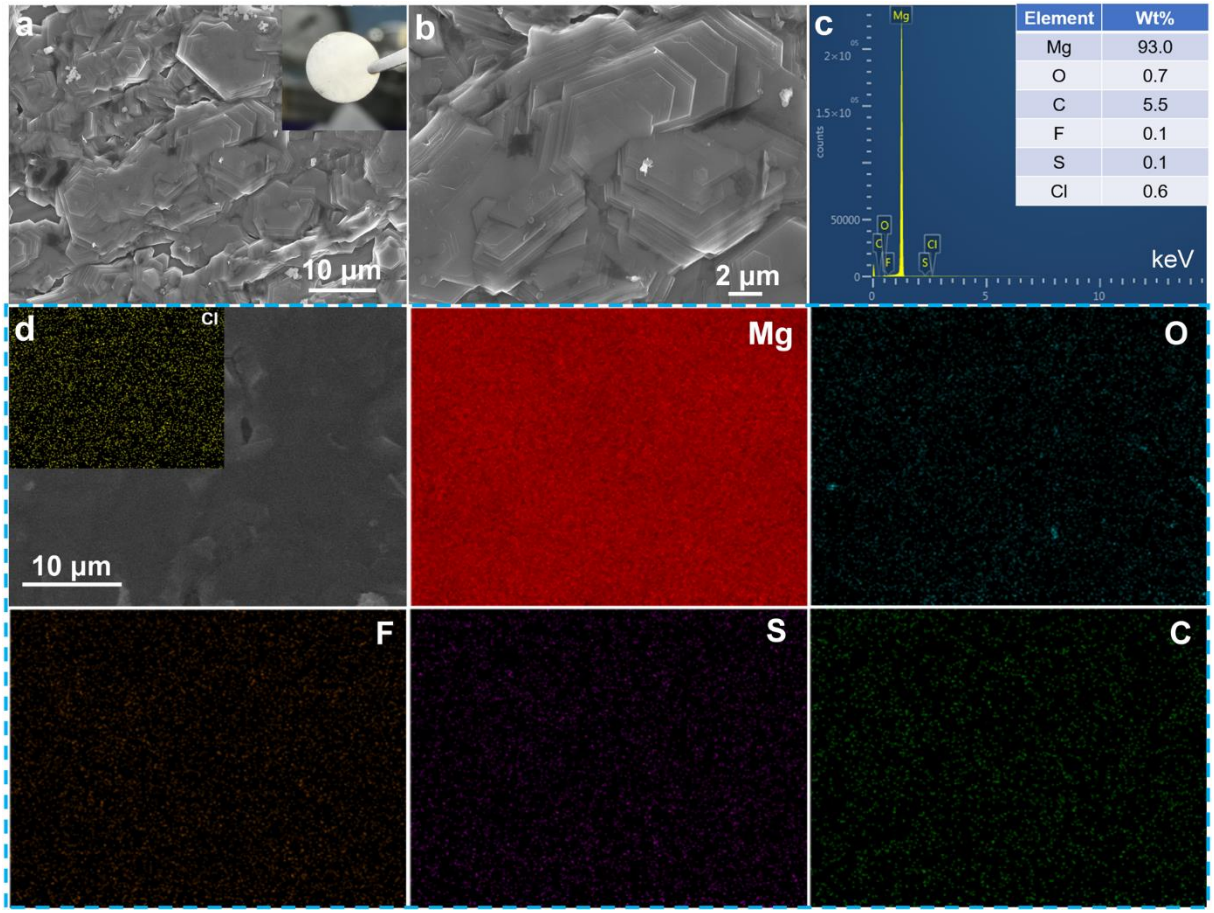


**Figure S15**. a-b) Typical SEM images (inset is the optical image) and the corresponding c) EDS spectrum and d) elemental mapping of the cycled Mg electrode from Mg//Mg symmetric cells in $Mg(OTf)_2$+ CP electrolyte at 0.5 mA $cm^{-2}$ and 0.5 mAh $cm^{-2}$.

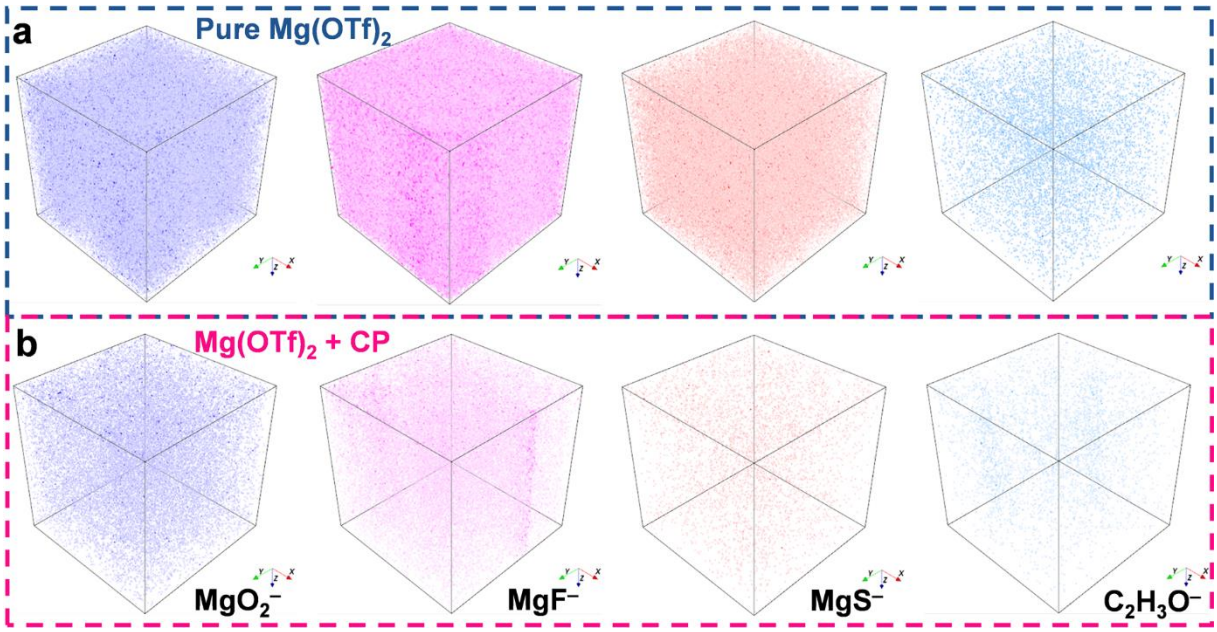


**Figure S16.** TOF-SIMS 3D render images of several secondary ion fragments ($MgO_2^-$, $MgF^-$, $MgS^-$ and $C_2H_3O^-$) from the cycled Mg electrodes in a) pure $Mg(OTf)_2$ and b) $Mg(OTf)_2$ + CP electrolytes.

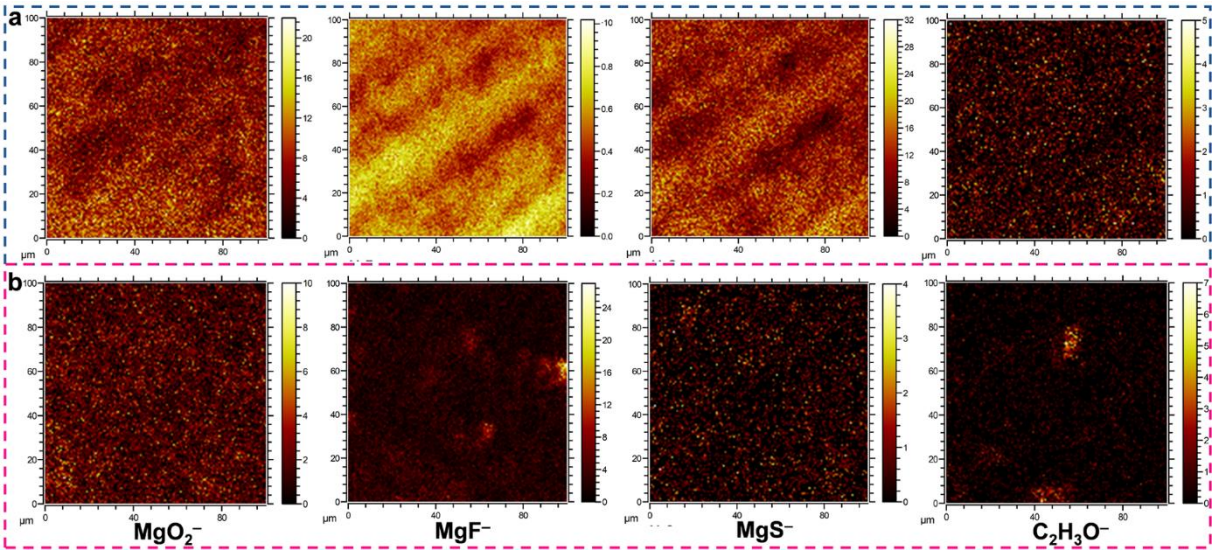


**Figure S17**. Cross-profile images of TOF-SIMS depth sputtering of several secondary ion fragments of $MgO_2^-$, $MgF^-$, $MgS^-$ and $C_2H_3O^-$ from the cycled Mg electrodes in a) pure $Mg(OTf)_2$ and b) $Mg(OTf)_2$ + CP electrolytes.

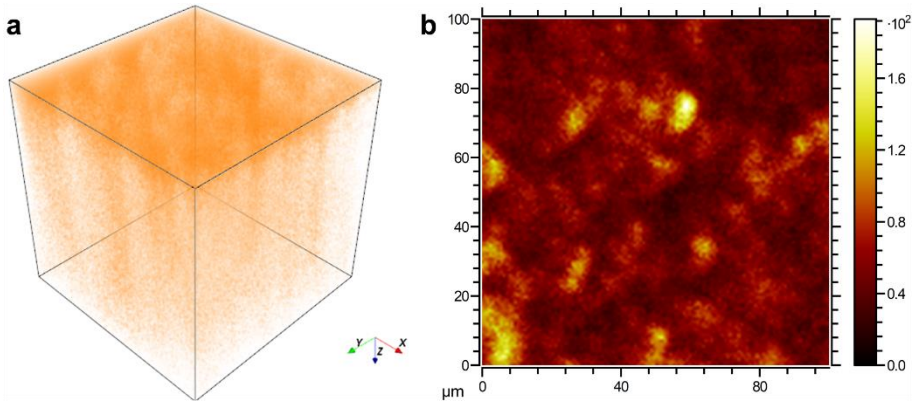


**Figure S18**. a) 3D render images and b) cross-profile images of TOF-SIMS depth sputtering of $Cl^-$ ion fragment from the cycled Mg electrode in $Mg(OTf)_2$ + CP electrolyte.

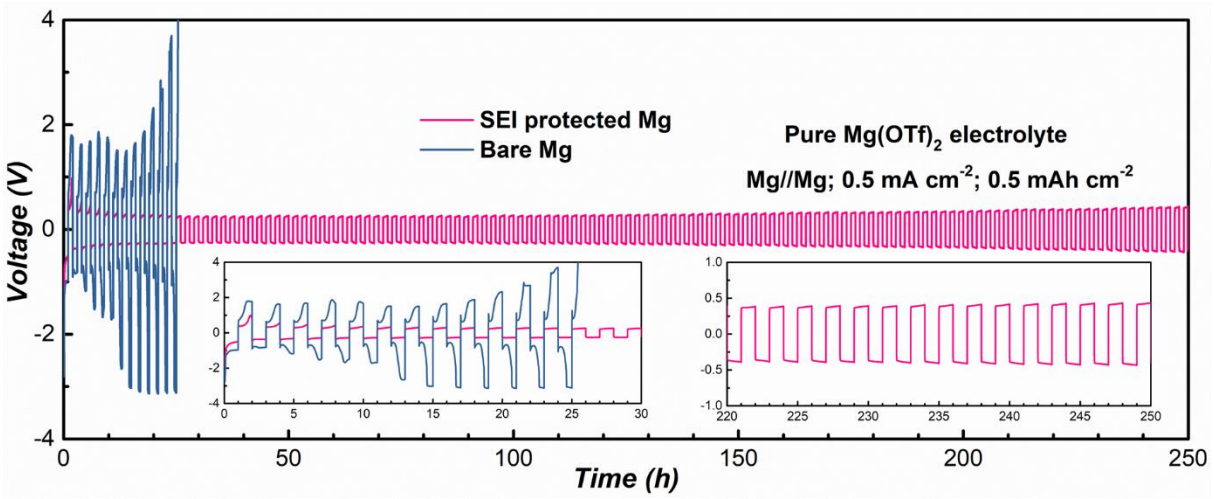


**Figure S19**. Voltage profiles of the pristine Mg and SEI-protected Mg anodes in $Mg(OTf)_2$ + CP electrolyte at 0.5 mA $cm^{-2}$ and 0.5 mAh $cm^{-2}$. Here, the bare Mg is polished Mg foil, and the SEI-protected Mg electrode is obtained from Mg//Mg cell cycled for 10 cycles in $Mg(OTf)_2$ + CP electrolyte.

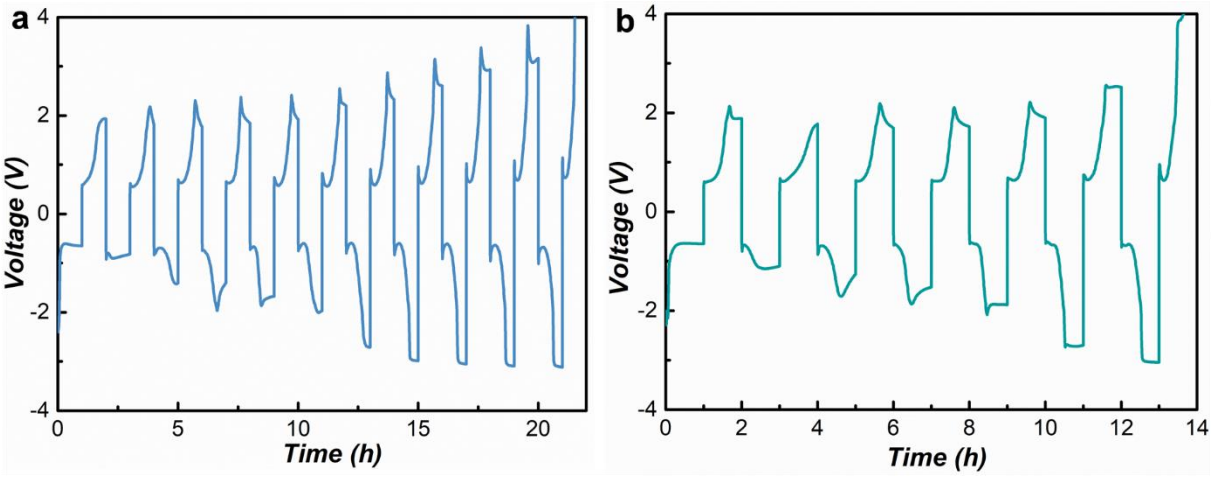


**Figure S20**. Voltage profiles of different cycled-Mg//cycled-Mg symmetric cells in pure $Mg(OTf)_2$ electrolyte at 0.5 mA $cm^{-2}$ and 0.5 mAh $cm^{-2}$. The cycled Mg electrodes are obtained from Mg//Mg cells after cycling in electrolytes of a) APC[12] and b) 0.3 M $Mg(OTf)_2$ + 0.2 M $MgCl_2$/DME.[1]

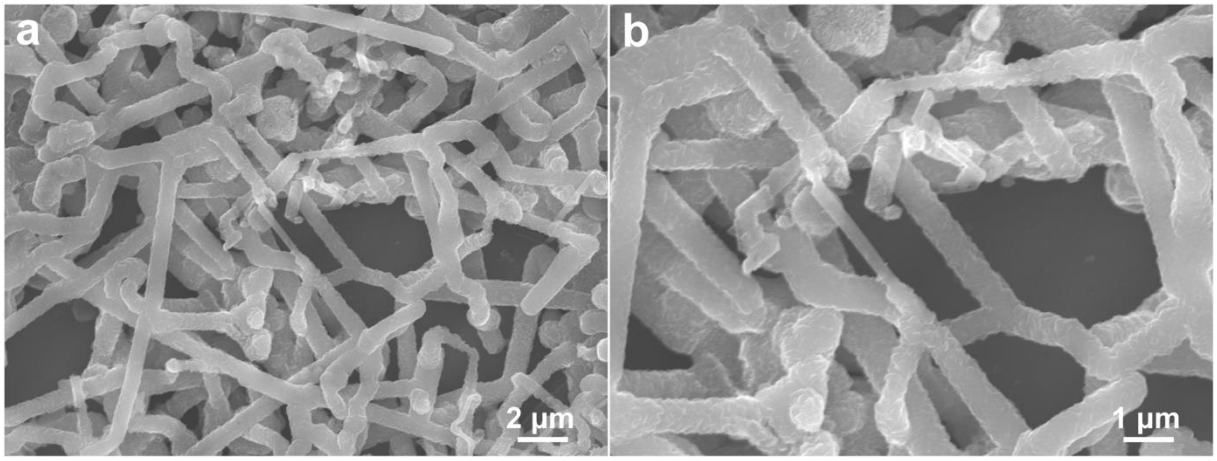


**Figure S21.** Typical SEM images of Mg deposits in pure $Mg(OTf)_2$ electrolyte at 0.5 mA $cm^{-2}$ and 0.5 mAh $cm^{-2}$.

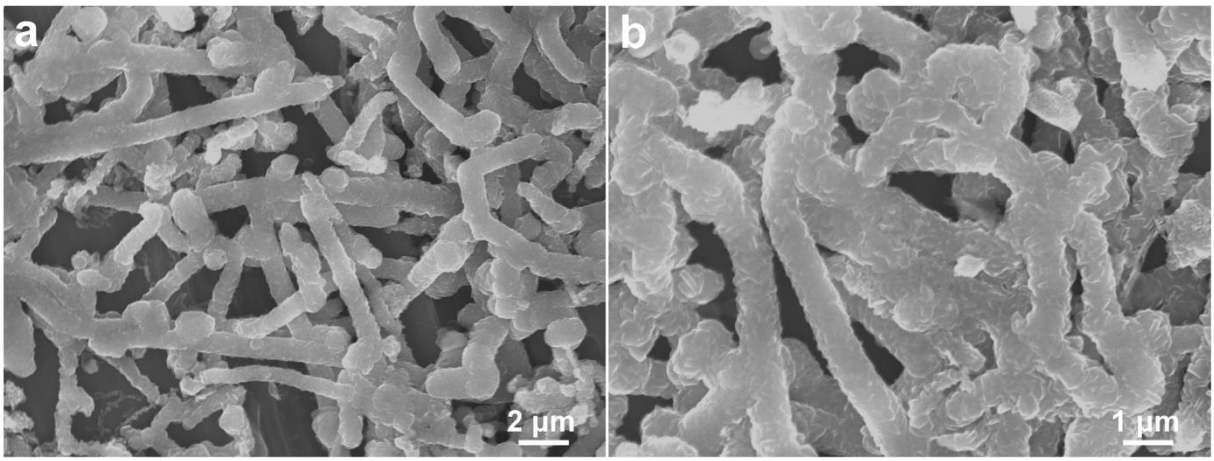


**Figure S22.** Typical SEM images of Mg deposits in pure $Mg(OTf)_2$ electrolyte at 1 mA $cm^{-2}$ and 1 mAh $cm^{-2}$.

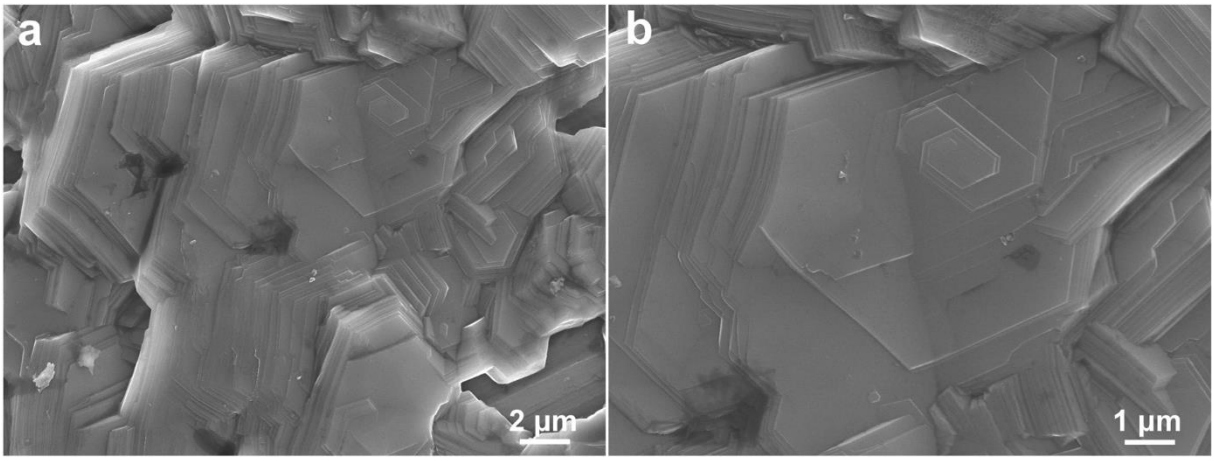


**Figure S23.** Typical SEM images of Mg deposits in $Mg(OTf)_2$ + CP electrolyte at 0.5 mA $cm^{-2}$ and 0.5 mAh $cm^{-2}$.

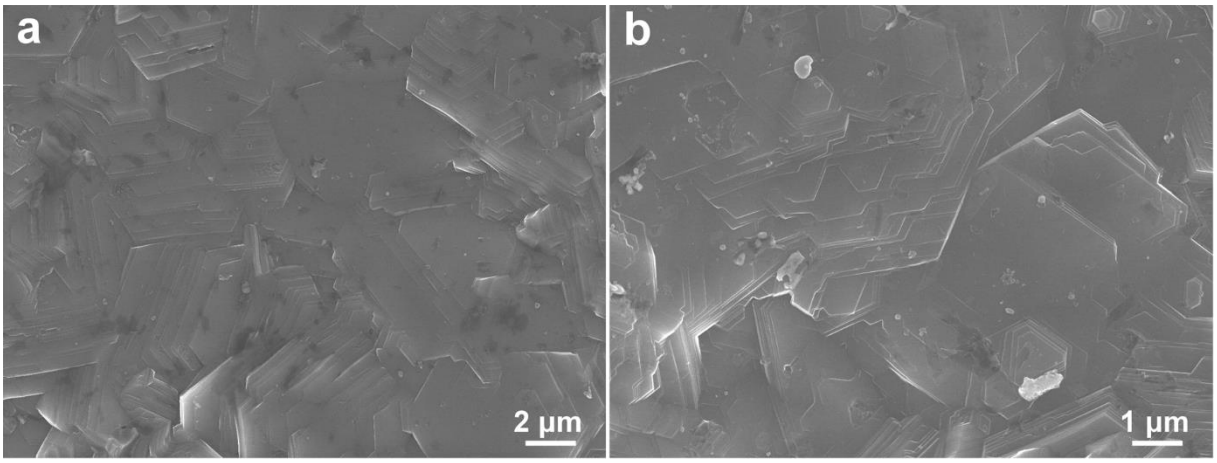


**Figure S24.** Typical SEM images of Mg deposits in $Mg(OTf)_2$ + CP electrolyte at 1 mA $cm^{-2}$ and 1 mAh $cm^{-2}$.

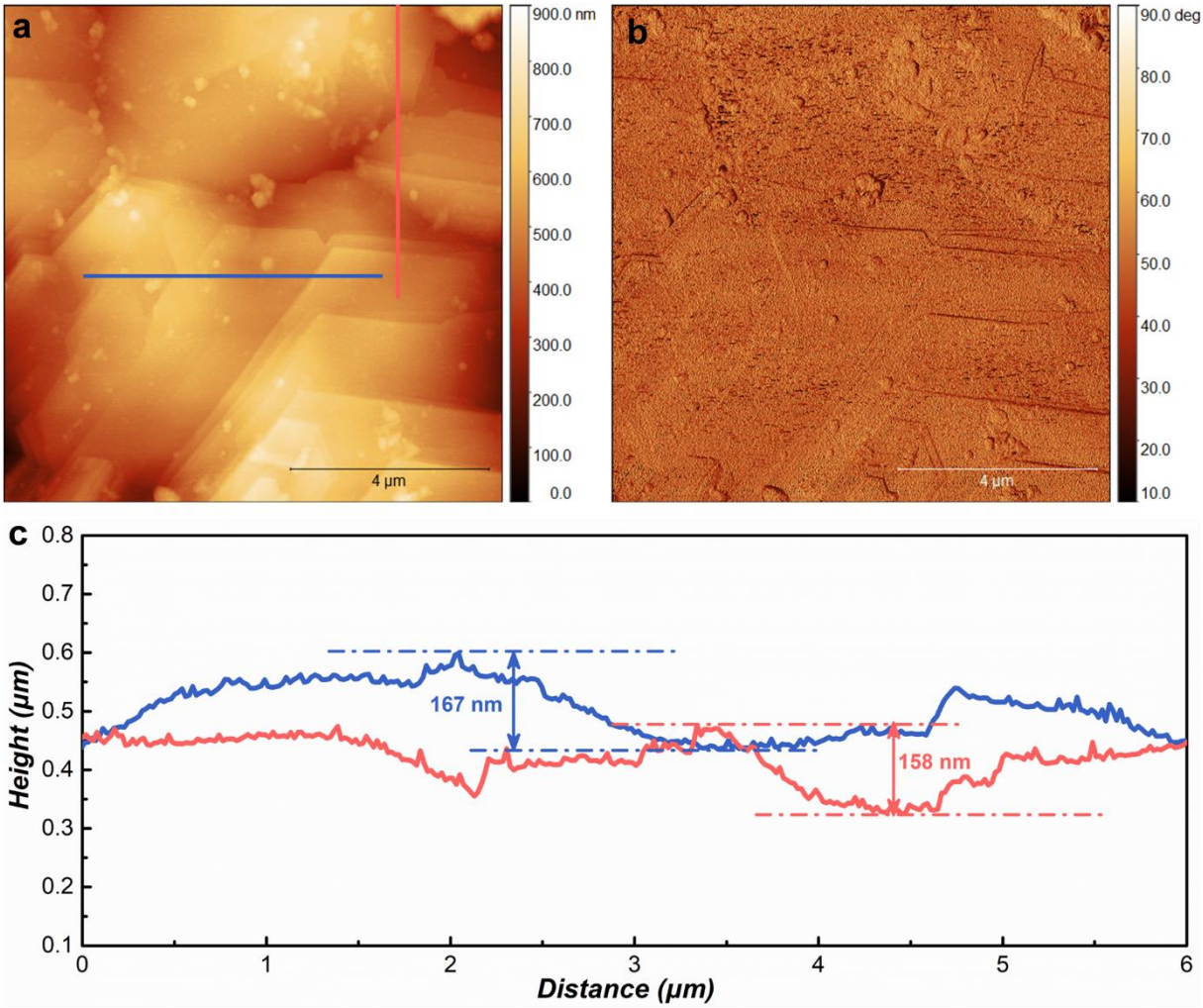


**Figure S25.** AFM characterization of Mg deposits at 0.5 mA $cm^{-2}$ and 0.5 mAh $cm^{-2}$ in $Mg(OTf)_2$ + CP electrolyte. a) height imaging; b) phase imaging and c) height profiles along X (blue) and Y(red) axis of Mg deposits on the surface.

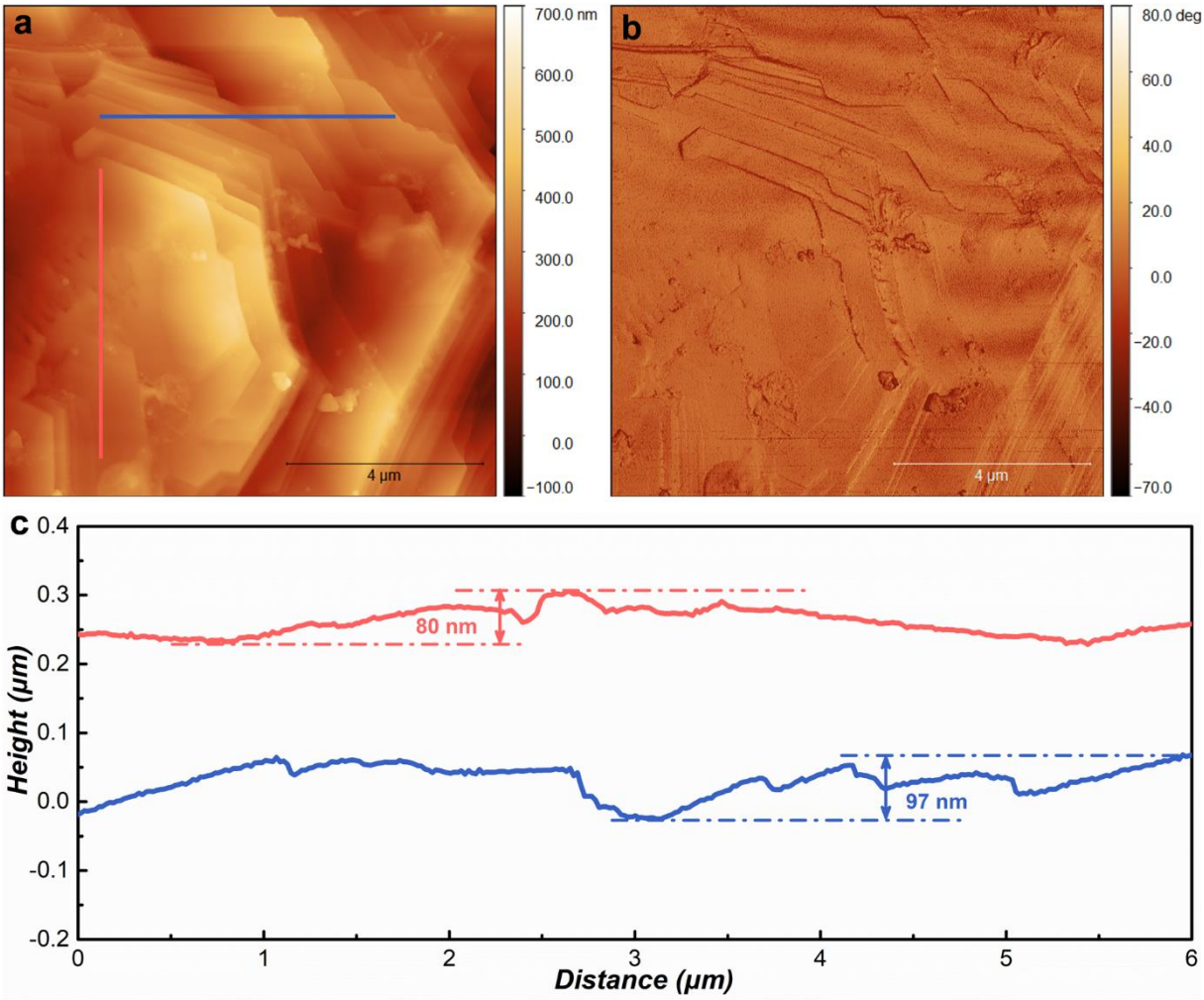


**Figure S26.** AFM characterization of Mg deposits at 1 mA $cm^{-2}$ and 1 mAh $cm^{-2}$ in $Mg(OTf)_2$ + CP electrolyte. a) height imaging; b) phase imaging and c) height profiles along X (blue) and Y(red) axis of Mg deposits on the surface.

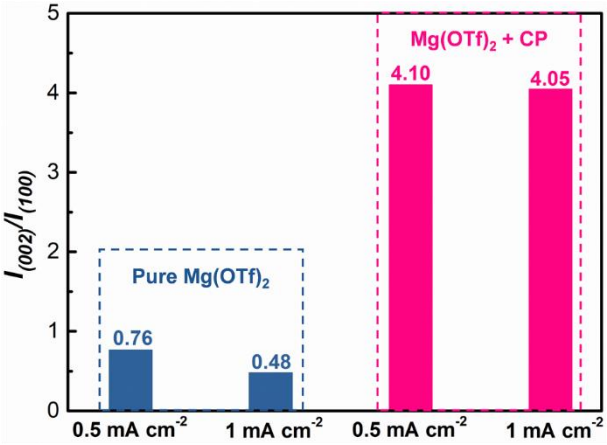


**Figure S27.** The calculated intensity ratio between Mg (002) and Mg (100) peaks of Mg deposits in different electrolytes.

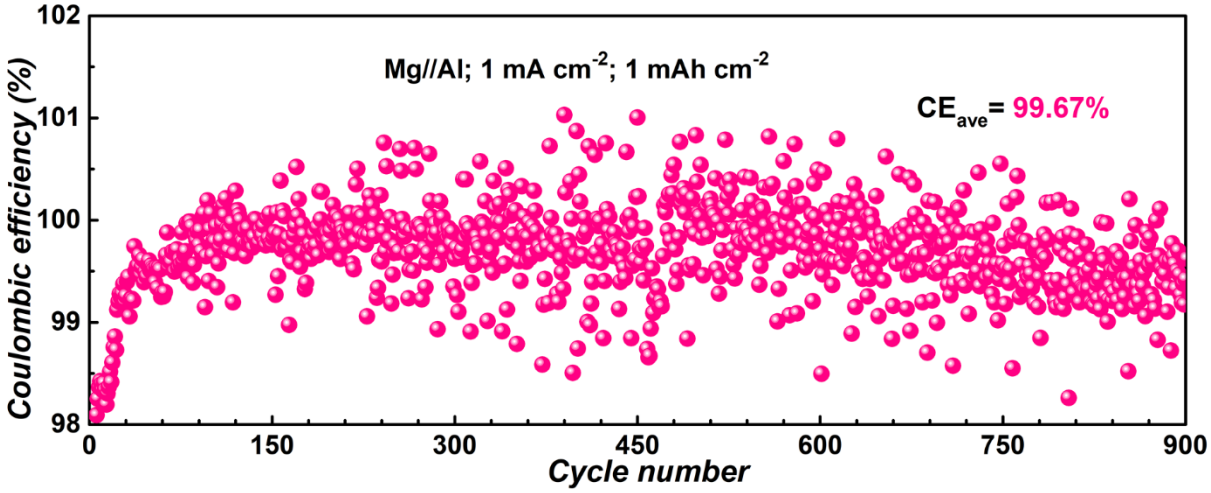


**Figure S28.** The enlarged Y ranges of the CE from Figure 3c in Mg//Al cells with $Mg(OTf)_2$ + CP electrolyte at 1 mA $cm^{-2}$/1 mAh $cm^{-2}$.

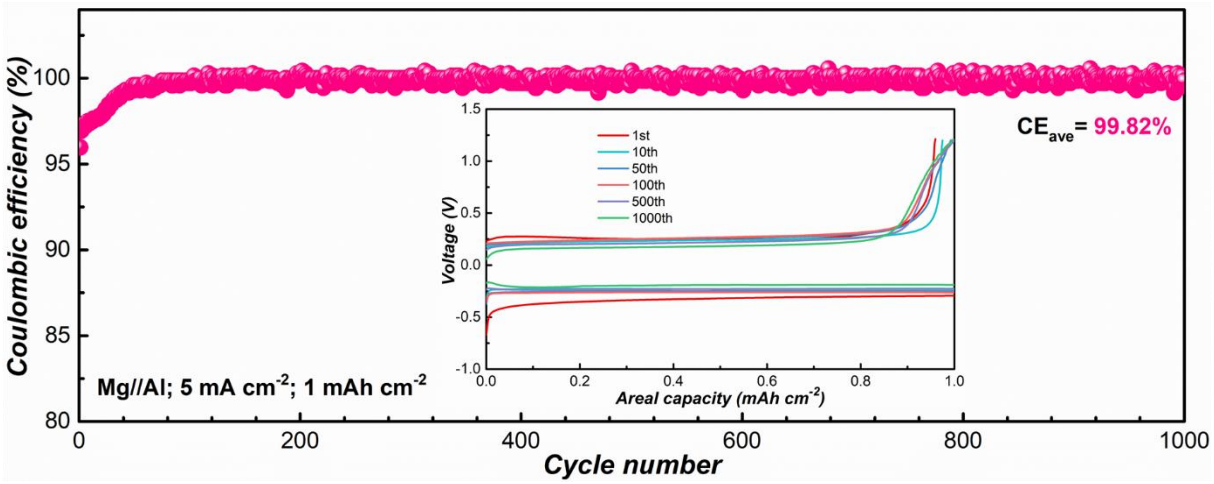


**Figure S29.** Plating/stripping CE of Mg//Al asymmetric cells using $Mg(OTf)_2$ + CP electrolyte at 5 mA $cm^{-2}$ and 1 mAh $cm^{-2}$. The inset is the corresponding voltage profiles from different cycles.

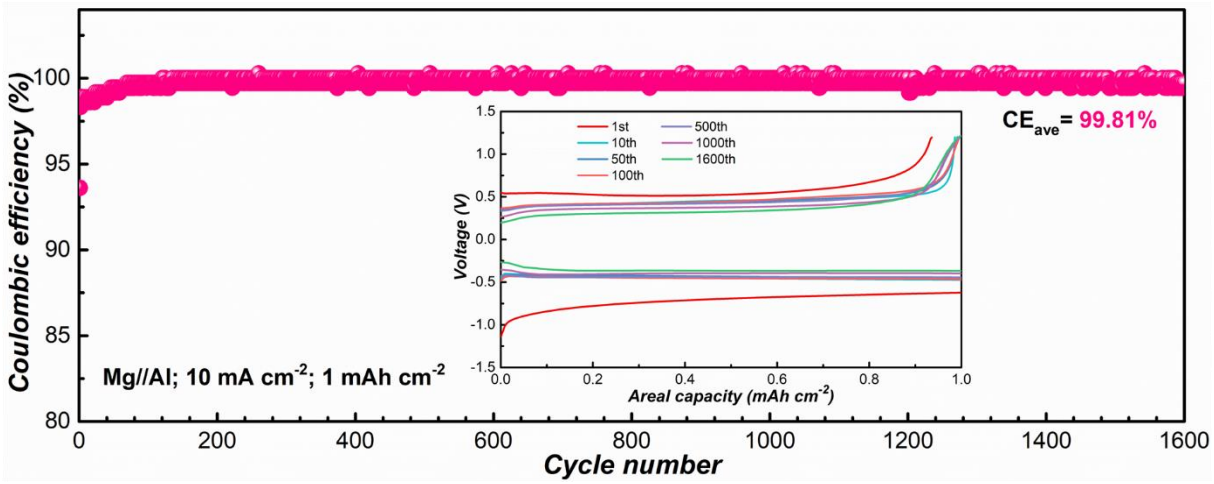


**Figure S30.** Plating/stripping CE of Mg//Al asymmetric cells using $Mg(OTf)_2$ + CP electrolyte at 10 mA $cm^{-2}$ and 1 mAh $cm^{-2}$. The inset is the corresponding voltage profiles from different cycles.

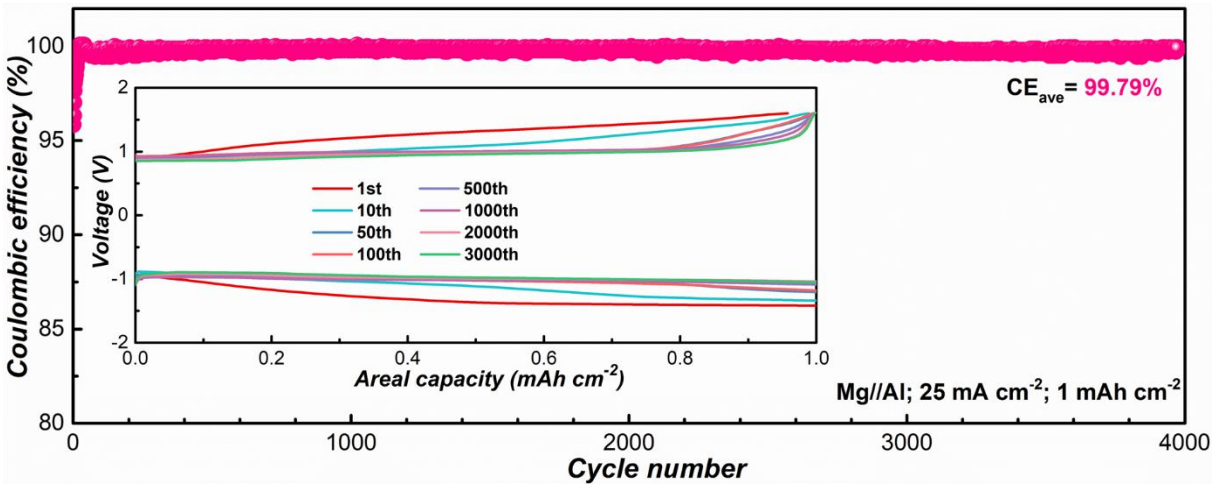


**Figure S31.** Plating/stripping CE of Mg//Al asymmetric cells using $Mg(OTf)_2$ + CP electrolyte at 25 mA $cm^{-2}$ and 1 mAh $cm^{-2}$. The inset is the corresponding voltage profiles from different cycles.

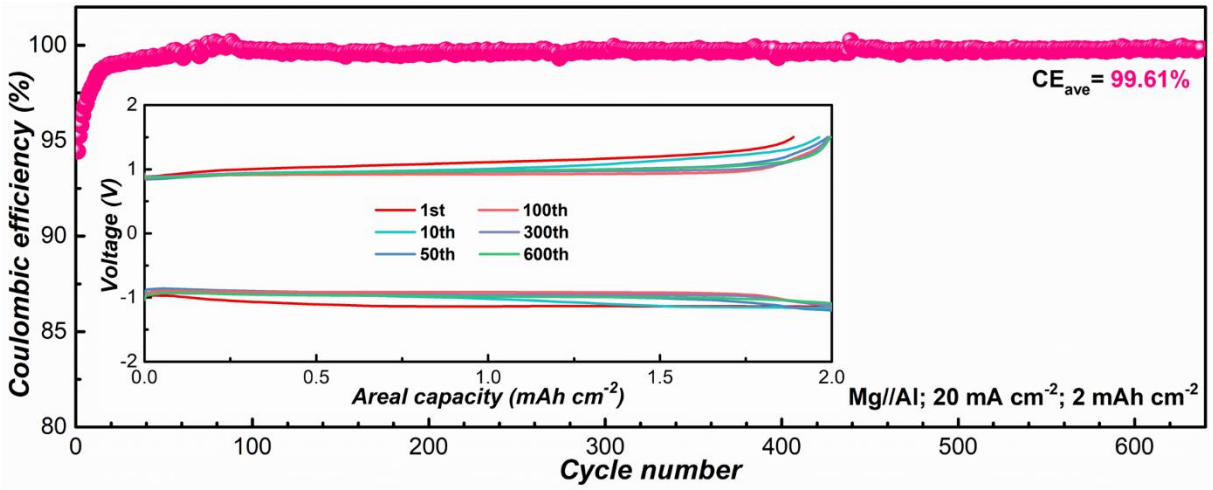


**Figure S32.** Plating/stripping CE of Mg//Al asymmetric cells using $Mg(OTf)_2$ + CP electrolyte at 20 mA $cm^{-2}$ and 2 mAh $cm^{-2}$. The inset is the corresponding voltage profiles from different cycles.

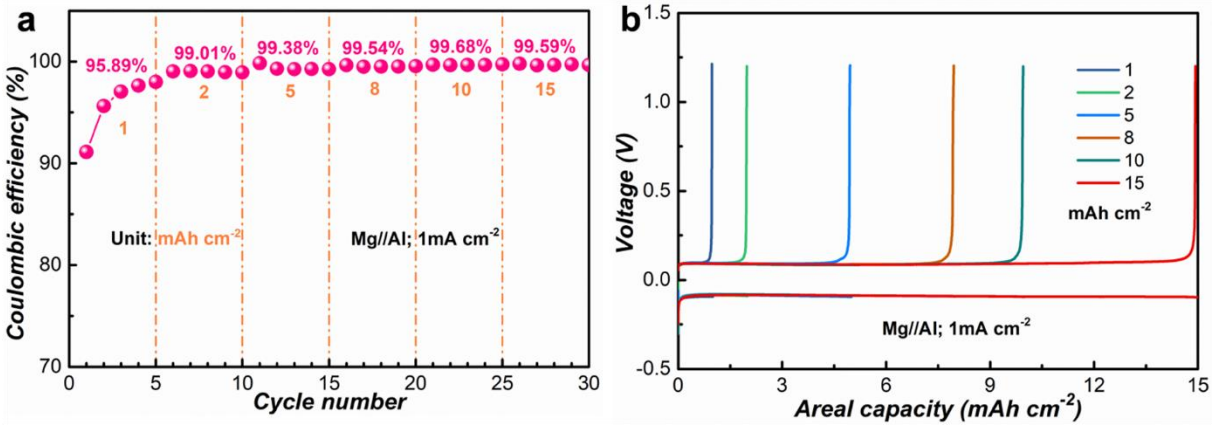


**Figure S33.** Galvanostatic Cycling of Mg//Al at different areal capacities using $Mg(OTf)_2$ + CP electrolyte. a) CEs and b) voltage profiles of cell cycled with a current density of 1 mA $cm^{-2}$ at areal capacities between 1 and 15 mAh $cm^{-2}$.

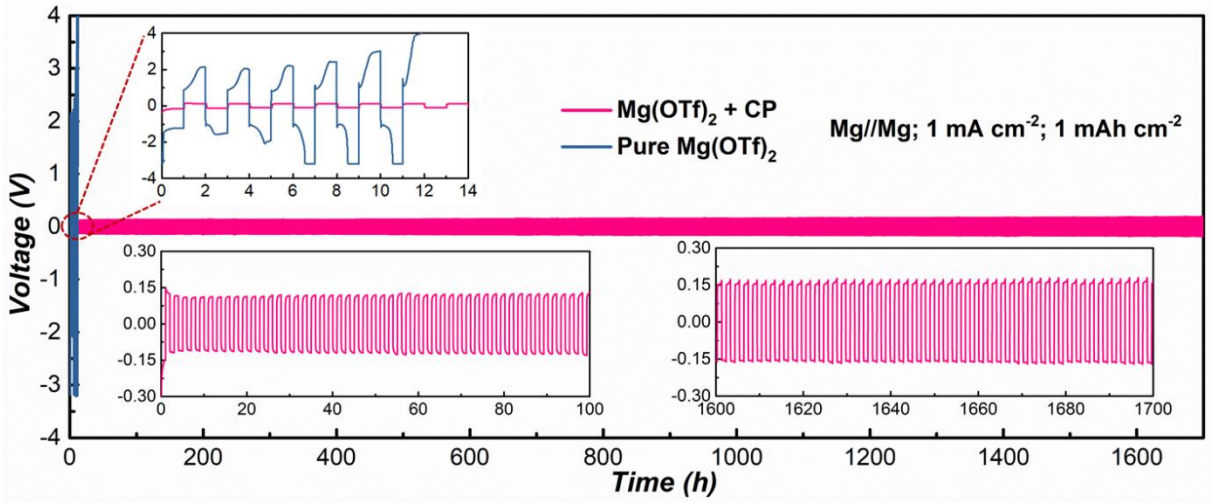


**Figure S34.** Comparison of cycling performance in symmetric cells with pure $Mg(OTf)_2$ and $Mg(OTf)_2$ + CP electrolytes at 1 mA $cm^{-2}$ and 1 mAh $cm^{-2}$. The insets are corresponding voltage profiles from different cycles.

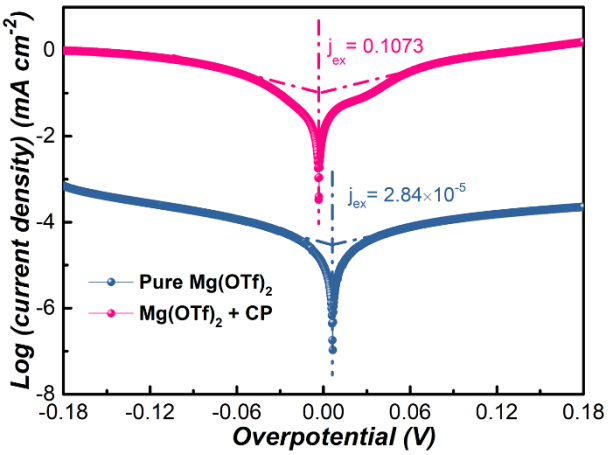


**Figure S35.** Tafel plots of Mg//Mg symmetrical cells with different electrolytes of pure $Mg(OTf)_2$ and $Mg(OTf)_2$ + CP.

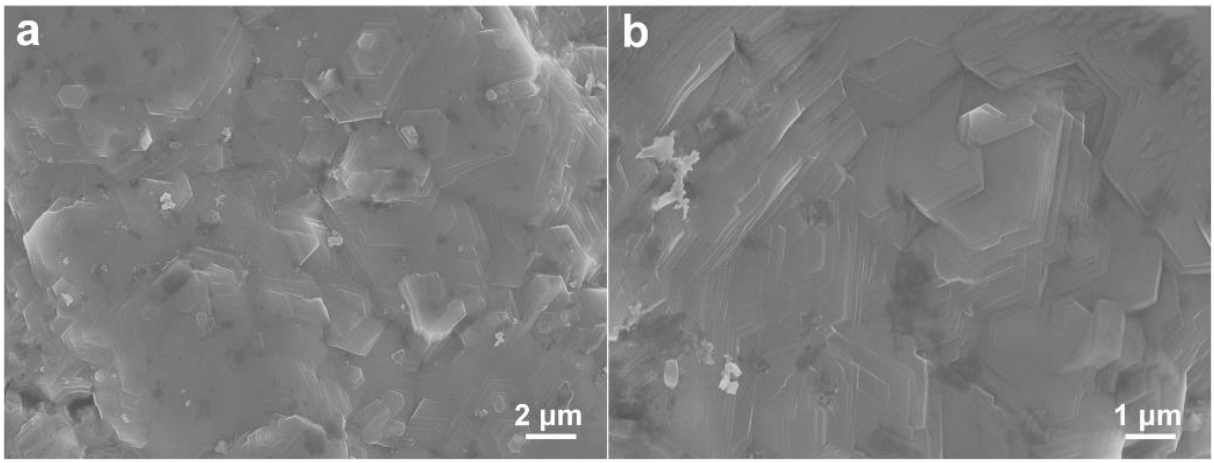


**Figure S36.** Top-view SEM images of the Mg electrode in $Mg(OTf)_2$ + CP electrolyte after 500 cycles at 1 mA $cm^{-2}$ and 1 mAh $cm^{-2}$.

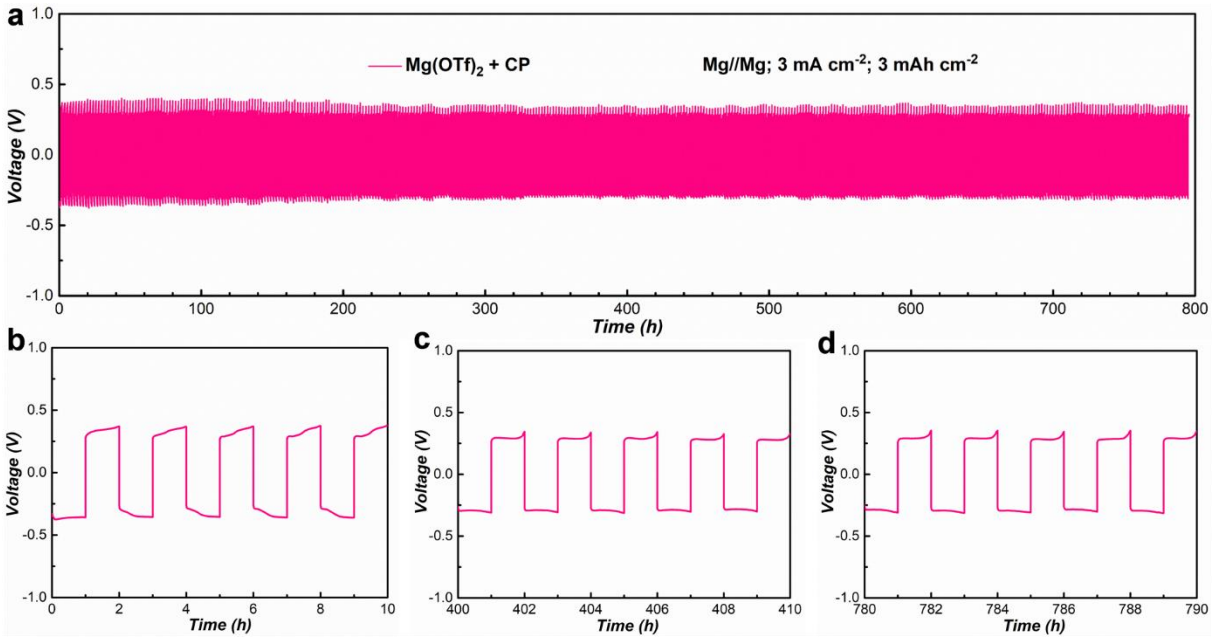


**Figure S37.** a) Galvanostatic cycling performance of Mg//Mg symmetric cell using $Mg(OTf)_2$ + CP electrolyte at 3 mA $cm^{-2}$ and 3 mAh $cm^{-2}$. Expanded voltage profiles at b) 0-10 h, c) 400-410 h and d) 780-790 h.

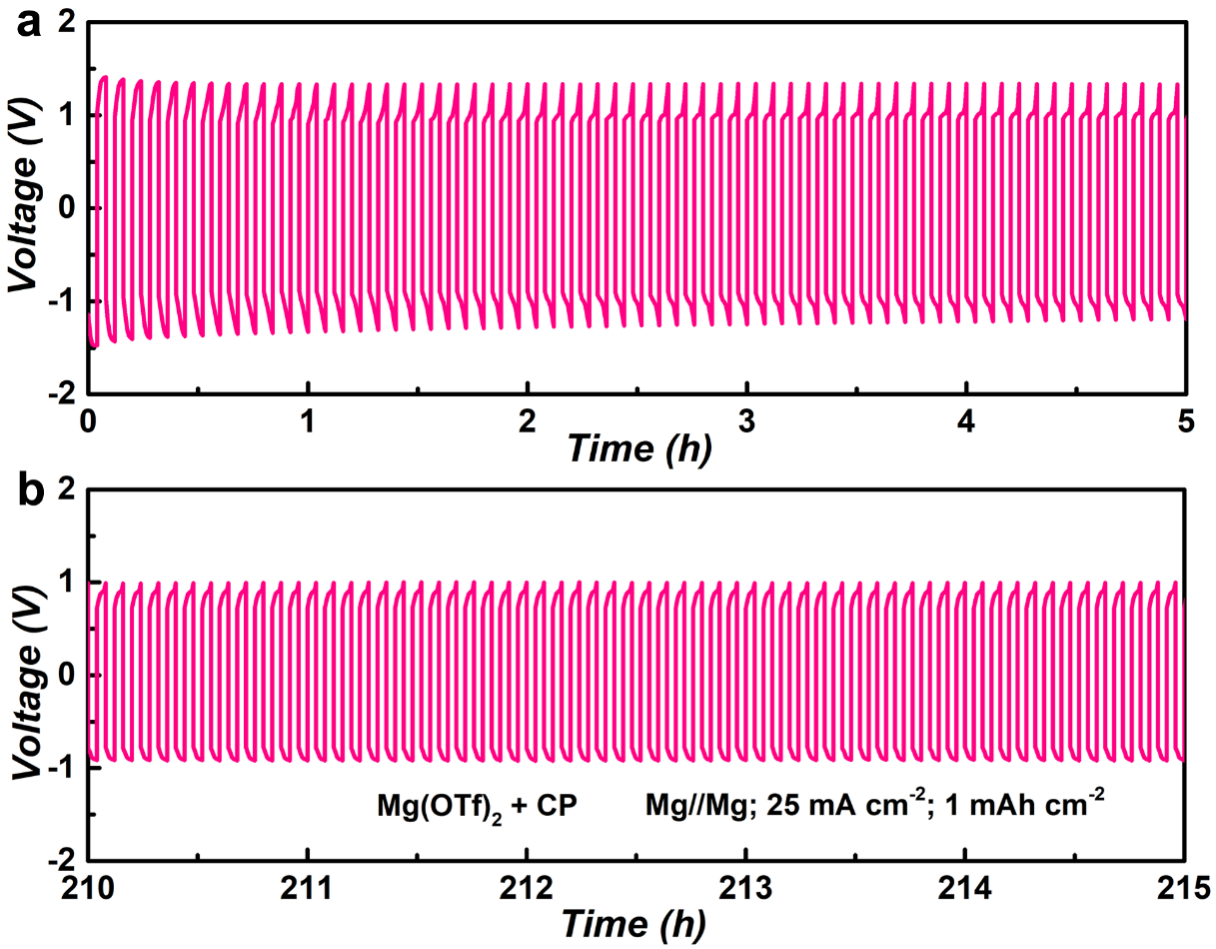


**Figure S38.** Expanded voltage profiles at a) 0-5 h and b) 210-215 h of Mg//Mg symmetric cell using $Mg(OTf)_2$ + CP electrolyte at 25 mA $cm^{-2}$ and 1 mAh $cm^{-2}$.

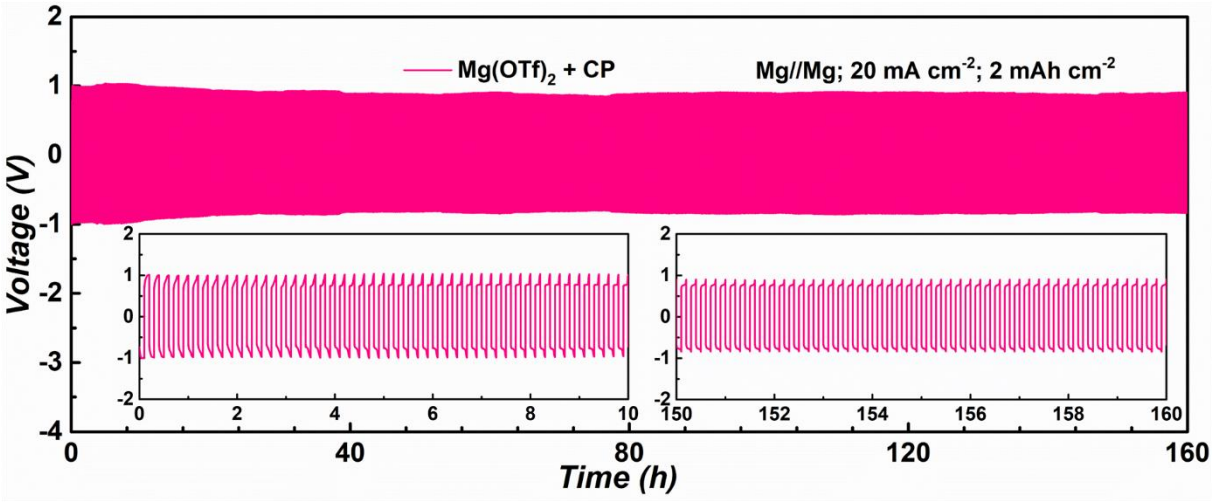


**Figure S39.** Galvanostatic cycling performance of Mg//Mg symmetric cell using $Mg(OTf)_2$ + CP electrolyte at 20 mA $cm^{-2}$ and 2 mAh $cm^{-2}$. The insets are expanded voltage profiles at 0-10 h and 150-160 h.

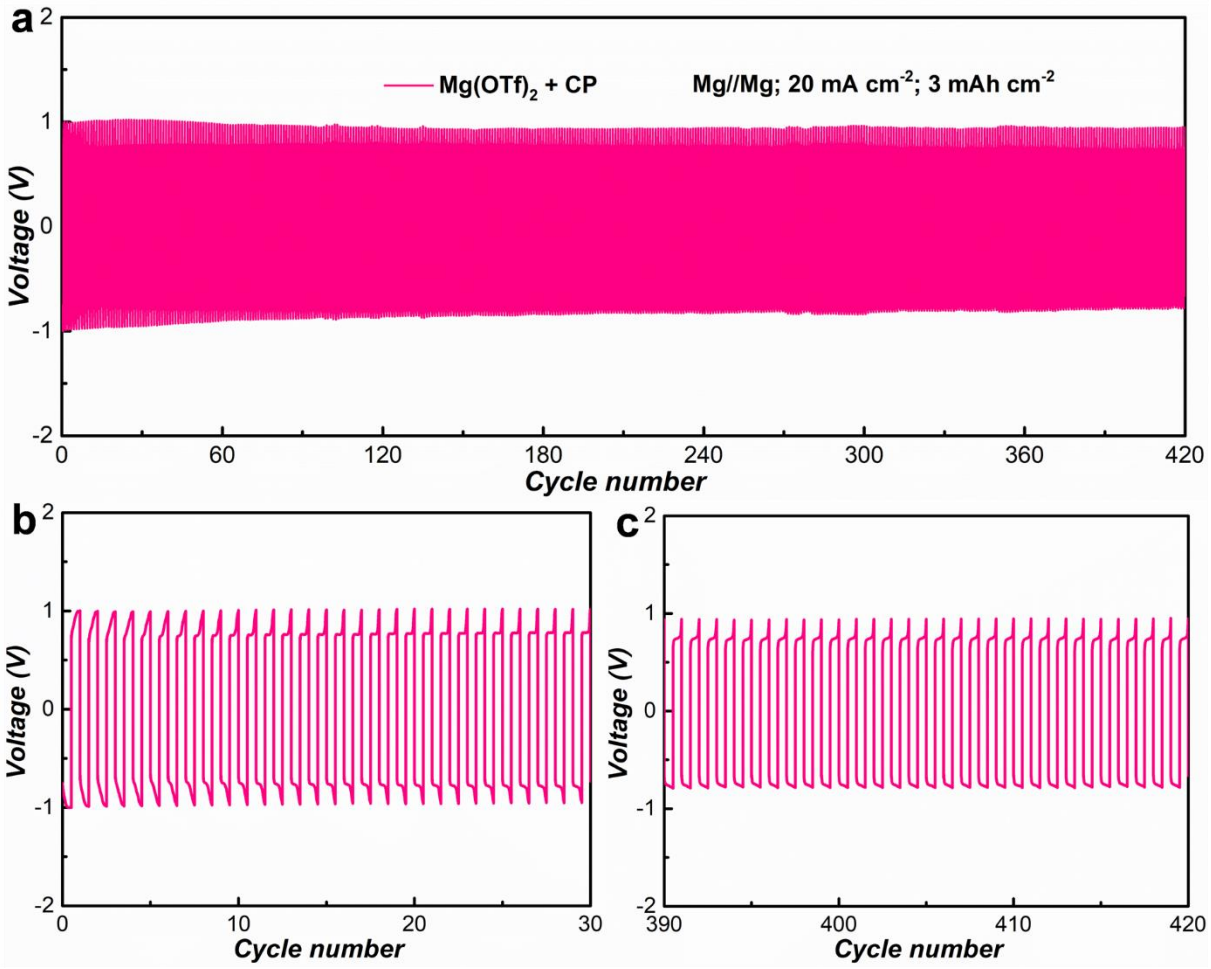


**Figure S40.** a) Galvanostatic cycling performance of Mg//Mg symmetric cell using $Mg(OTf)_2$ + CP electrolyte at 20 mA $cm^{-2}$ and 3 mAh $cm^{-2}$. Expanded voltage profiles at b) 0-30 cycles, and c) 390-420 cycle.

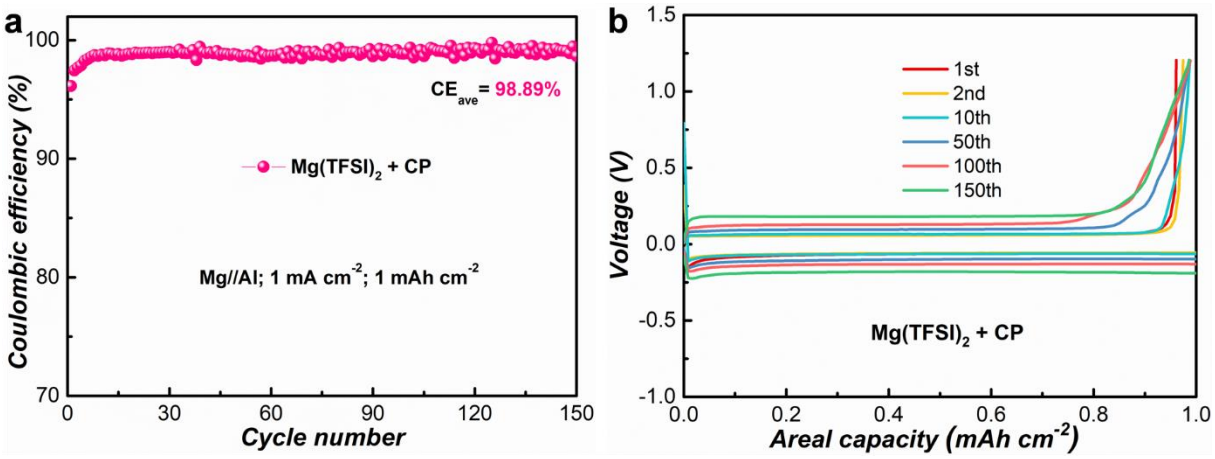


**Figure S41.** a) Plating/stripping CE and b) selected voltage profiles of Mg//Al asymmetric cells using $Mg(TFSI)_2$ + CP electrolyte at 1 mA $cm^{-2}$ and 1 mAh $cm^{-2}$.

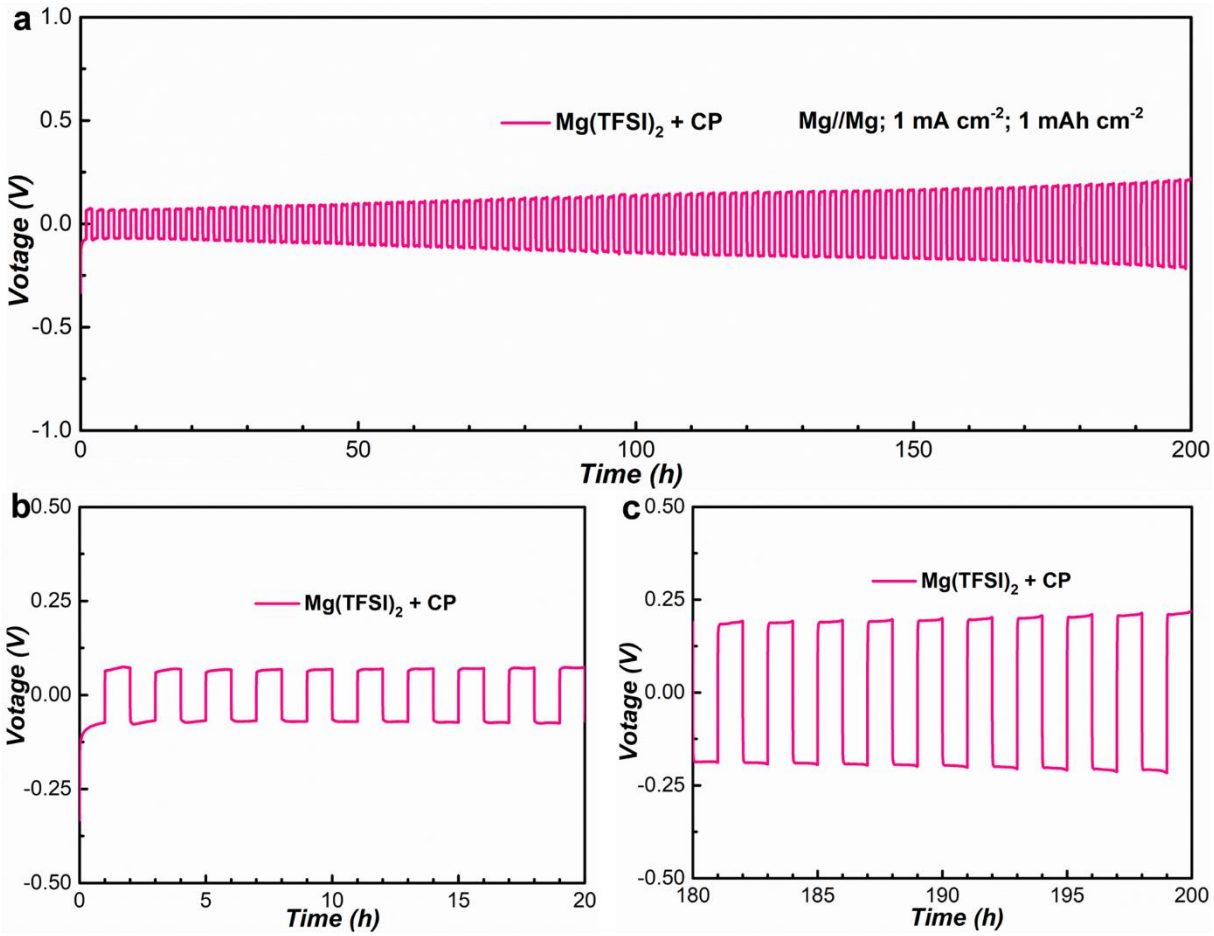


**Figure S42.** a) Galvanostatic cycling performance of Mg//Mg symmetric cell using $Mg(TFSI)_2$ + CP electrolyte at 1 mA $cm^{-2}$ and 1 mAh $cm^{-2}$. Expanded voltage profiles at b) 0-20 h, and c) 180-200 h.

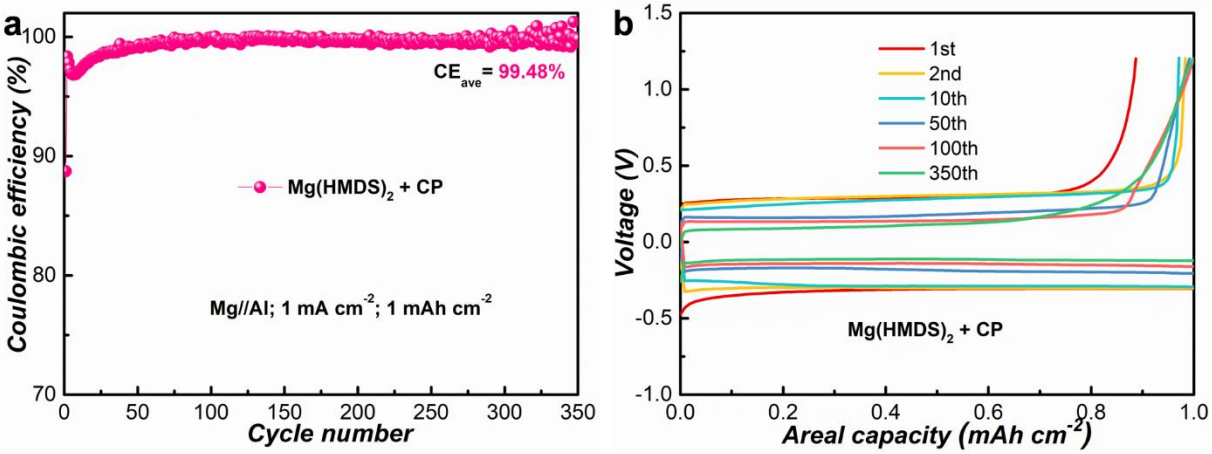


**Figure S43.** a) Plating/stripping CE and b) selected voltage profiles of Mg//Al asymmetric cells using $Mg(HMDS)_2$ + CP electrolyte at 1 mA $cm^{-2}$ and 1 mAh $cm^{-2}$.

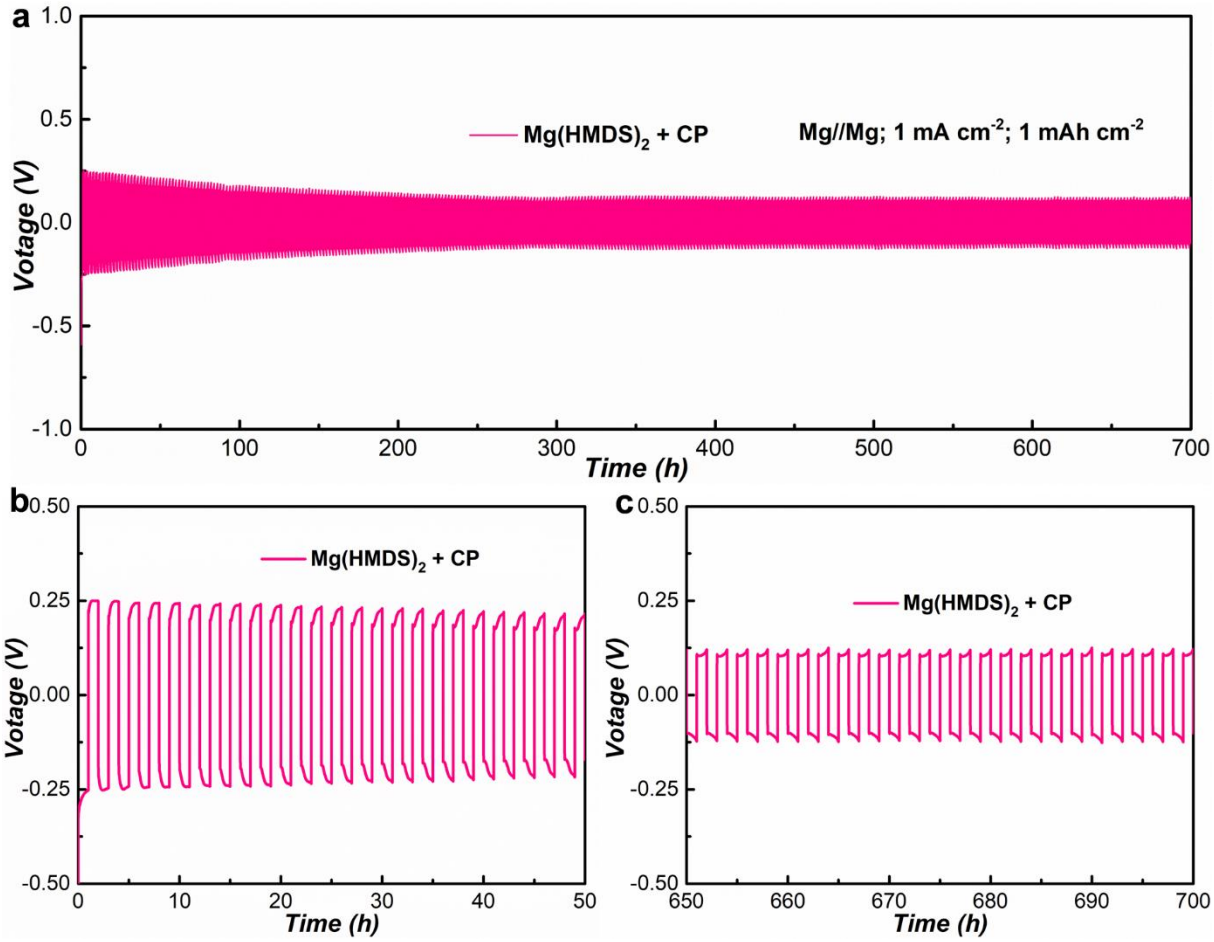


**Figure S44.** a) Galvanostatic cycling performance of Mg//Mg symmetric cell using $Mg(HMDS)_2$ + CP electrolyte at 1 mA $cm^{-2}$ and 1 mAh $cm^{-2}$. Expanded voltage profiles at b) 0-50 h, and c) 650-700 h.

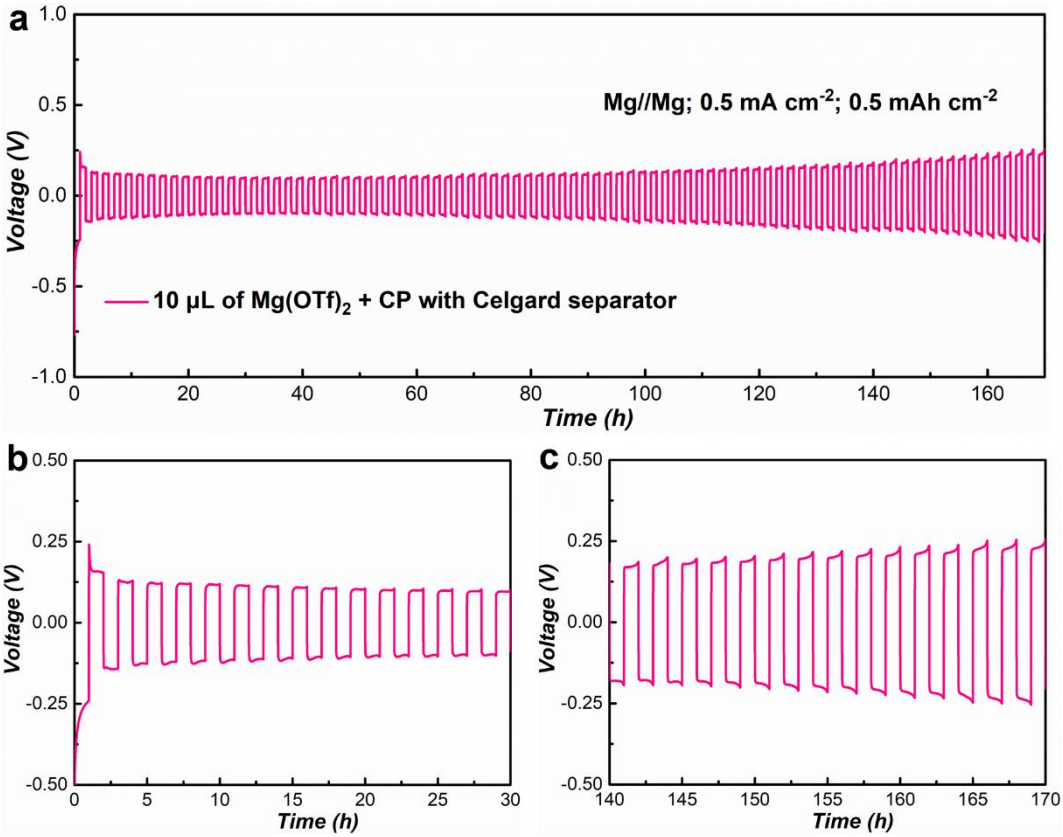


**Figure S45.** a) Galvanostatic cycling performance of Mg//Mg symmetric cell using 10 µl of $Mg(OTf)_2$ + CP electrolyte with Celgard separator at 0.5 mA $cm^{-2}$ and 0.5 mAh $cm^{-2}$. Expanded voltage profiles at b) 0-30 h, and c) 140-170 h.

Note to Figure S45: In order to investigate the limitation of the electrolyte with ultra-low quantity, we have tried to assemble the coin cells with a low quantity of electrolyte (10 µL). As the electrolyte amount of 10 µL is too low to infiltrate the GF separator for ion transport, the Celgard separator was used for instead. As shown in Figure S45, the Mg//Mg cell can be cycled for 170 h with a low overpotential of ~ 0.1 V at 0.5 mA $cm^{-2}$ and 0.5 mAh $cm^{-2}$ using 10 µL of $Mg(OTf)_2$ + CP electrolyte. The overpotential is similar compared with the cell using GF separator, indicating that the amount of electrolyte would not change the reaction kinetics. However, it is notable that the duration of the cell with 10 µL of electrolyte is not as good as the cell with the normal configuration. As the electrolyte keeps being continuously consumed along with cycling, the electrolyte may be insufficient to maintain the low internal resistance if the added amount is low, resulting in relatively shorter cycling duration and gradually increased

overpotentials. Therefore, it is very necessary and important to optimize the electrolyte amounts during the battery assembly to balance the cycling performance and the cell weight for the practical applications.

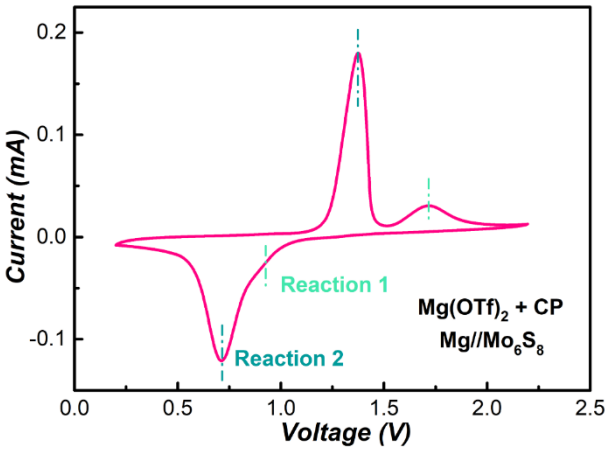


**Figure S46.** The typical CV curve of Mg//$Mo_6S_8$ cell with $Mg(OTf)_2$ + CP electrolyte at a scan rate of 0.1 mV $s^{-1}$ in the potential range of 0.2-2.2 V (versus $Mg/Mg^{2+}$).

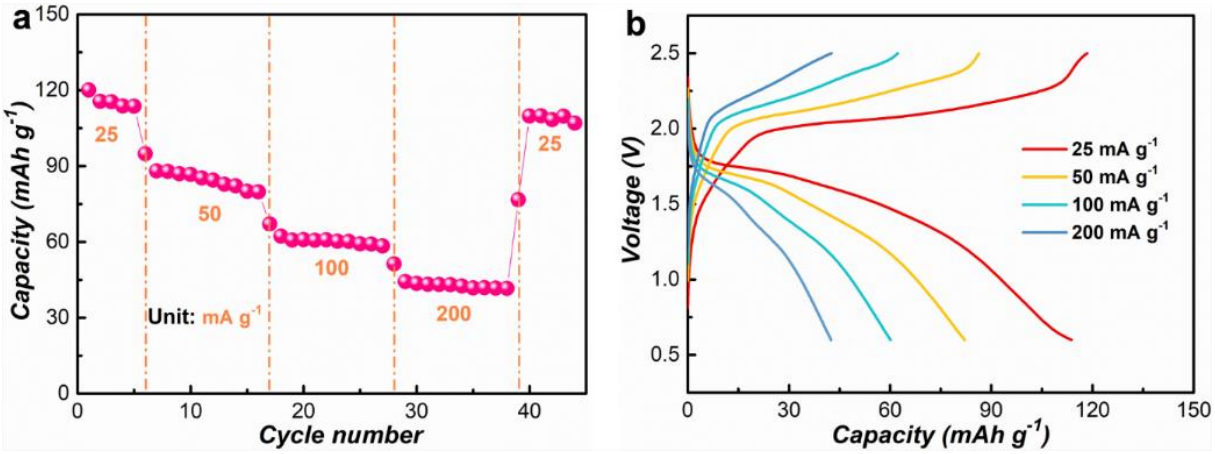


**Figure S47.** Rate performance of Mg//PTCDA cells with $Mg(OTf)_2$ + CP electrolyte from 25 to 200 mA $g^{-1}$ and b) the corresponding charging/discharging profiles between 0.6 V and 2.5 V (versus $Mg/Mg^{2+}$).

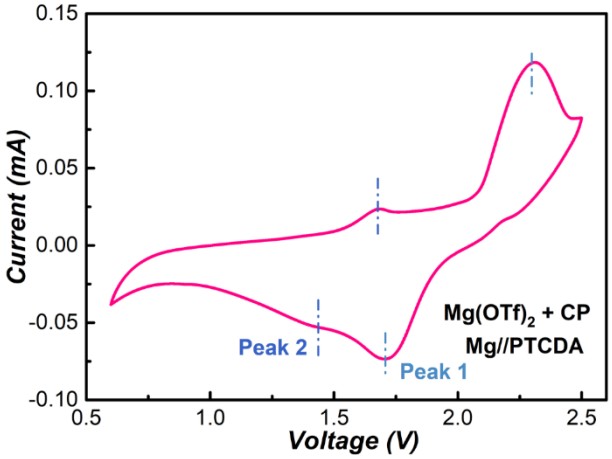


**Figure S48.** The typical CV curve of the Mg//PTCDA cell with $Mg(OTf)_2$ + CP electrolyte at a scan rate of 0.1 mV $s^{-1}$.

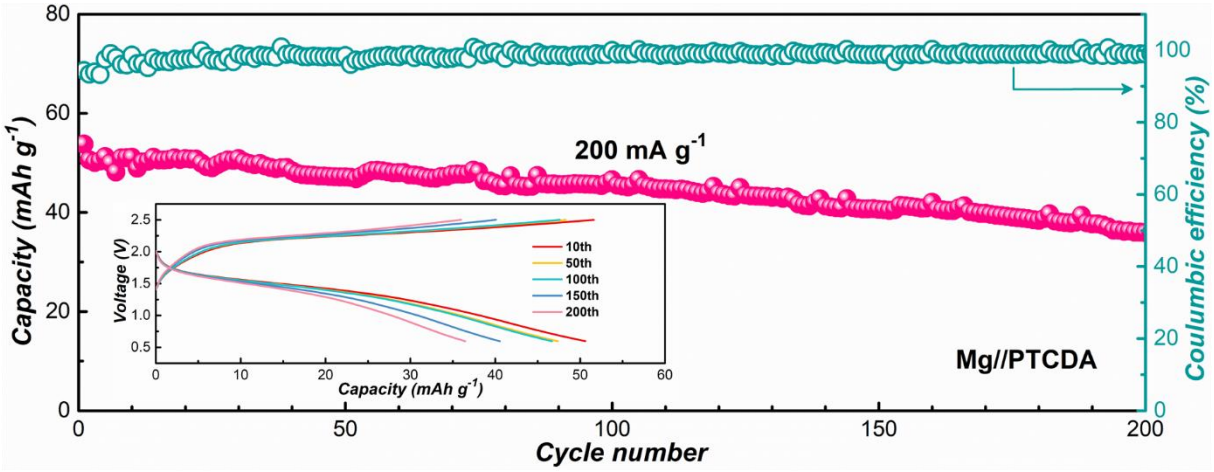


**Figure S49.** Cycling performance of Mg//PTCDA cells at a current density of 200 mA $g^{-1}$. The inset is the selected charging/discharging profiles between 0.6 V and 2.5 V (versus $Mg/Mg^{2+}$).

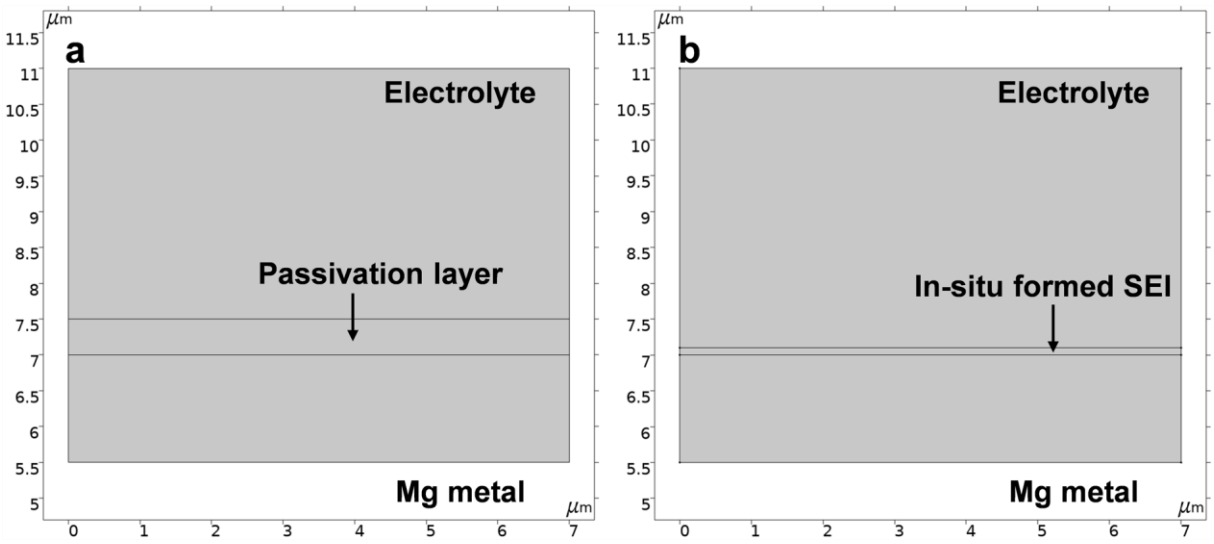


**Figure S50.** 2D geometric model and size of Mg deposits in electrolytes of a) pure $Mg(OTf)_2$ and b) $Mg(OTf)_2$ + CP at a current density of 0.5 mA $cm^{-2}$.

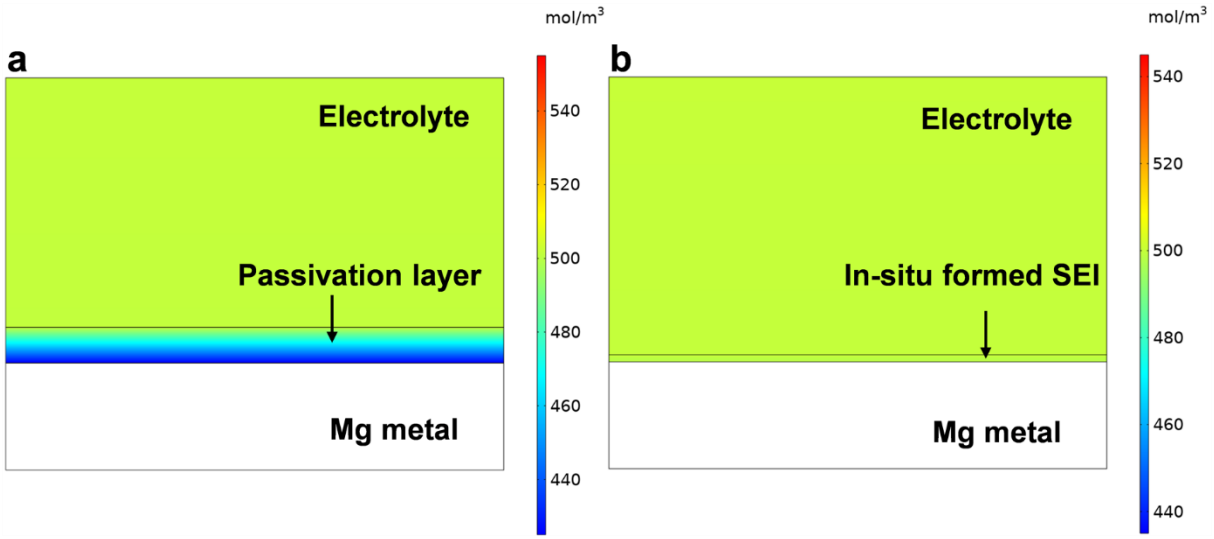


**Figure S51**. COMSOL simulation of the $Mg^{2+}$ flux distribution on Mg electrodes in different electrolytes of a) pure $Mg(OTf)_2$ and c) $Mg(OTf)_2$ + CP at a current density of 0.5 mA $cm^{-2}$.

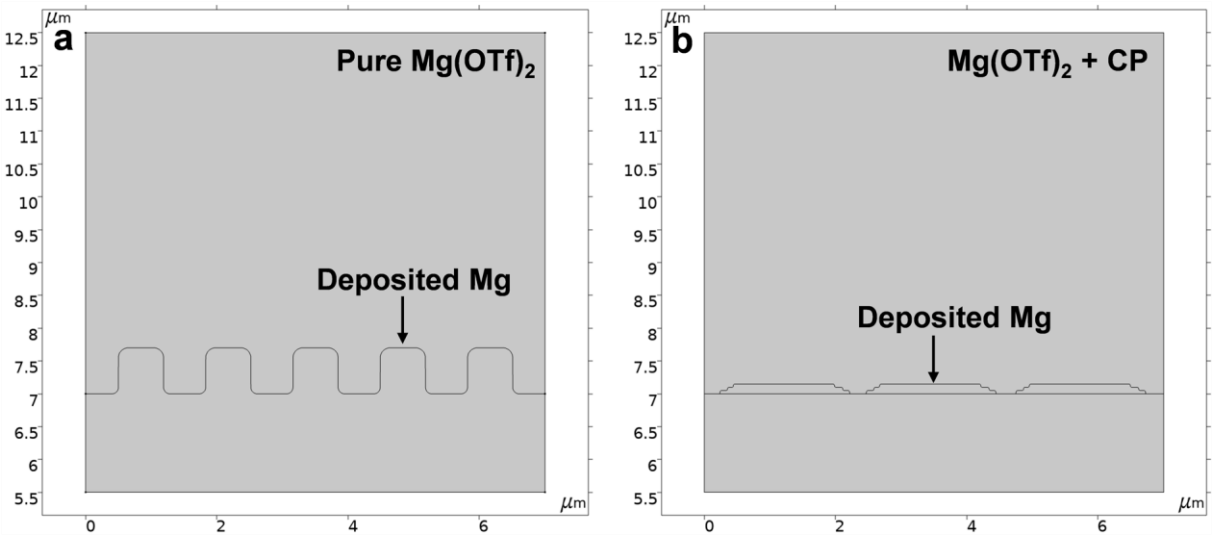


**Figure S52**. 2D geometric model and size of Mg deposits in electrolytes of a) pure $Mg(OTf)_2$ and b) $Mg(OTf)_2$ + CP at a current density of 0.5 mA $cm^{-2}$.

**Table S1.** Fitting results of EIS results in Figure S9 for symmetric cells with $Mg(OTf)_2$ + CP electrolyte after different cycles at 0.5 mA $cm^{-2}$ and 0.5 mAh $cm^{-2}$.

| **$Mg(OTf)_2$ + CP electrolyte** | **$R_s$ (Ω)** | **$R_{SEI}$ (Ω)** | **$R_{ct}$ (Ω)** |
|---|---|---|---|
| **Before cycling** | 27.92 | 3591 | $1.012\times10^4$ |
| **After 1st cycle** | 31.44 | 102.4 | 2897 |
| **After 10th cycle** | 31.84 | 47.29 | 254.4 |
| **After 50th cycle** | 37.08 | 59.75 | 489.1 |
| **After 100th cycle** | 38.65 | 56.31 | 472.7 |

**Table S2.** Performance comparison of the reported asymmetric cells in different Mg electrolytes.

| Electrolyte | Current density (mA $cm^{-2}$) | Areal capacity (mAh $cm^{-2}$) | Cycles | Average CE (%) |
|---|---|---|---|---|
| LBhfip/DME[13] | 0.5 | 0.5 | 500 | 99.0 |
| $Mg[B(Otfe)_4]_2$/DME[14] | 0.5 | 0.5 | 100 | 98.17 |
| $Mg(OTf)_2$ +$MgCl_2$/DME[1] | 0.5 | 0.5 | 100 | 99.1 |
| $Mg(OTf)_2$+TBAC/DME[15] | 0.5 | 0.5 | 200 | 97.7 |
| $Mg(OTf)_2$ +$InCl_3$/DME[16] | 0.5 | 0.5 | 250 | 98.7 |
| $Mg(HMDS)_2$+$MgBr_2$+ $TBABH_4$/DME[17] | 0.5 | 0.5 | 1000 | 99.26 |
| $Mg(HMDS)_2$+$TBABH_4$/ DME[18] | 0.5 | 0.5 | 150 | 98.5 |
| $Mg(pftb)_2$+$MgCl_2$/THF[19] | 0.5 | 0.5 | 3200 | ~99.7 |
| MLCC-1T1B[20] | 5 | 2 | 1500 | ~99.9 |
| $Mg(TFSI)_2$+M4/DME[21] | 0.1 | 0.1 | 100 | 99.5 |
| $Mg(TFSI)_2$+$MgCl_2$/DME+ THF[22] | 1 | 1 | / | 98.8 |
| **$Mg(OTf)_2$ + CP/DME (this work)** | **0.5** | **0.5** | **700** | **99.59** |
| | **1** | **1** | **900** | **99.67** |
| | **10** | **1** | **1600** | **99.81** |
| | **25** | **1** | **4000** | **99.79** |
| | **20** | **2** | **640** | **99.61** |

**Table S3.** Performance comparison of the reported symmetric cells in different Mg electrolytes.

| Electrolyte | Current density (mA $cm^{-2}$) | Areal capacity (mAh $cm^{-2}$) | Overpotential (mV) | Cycling life (h) | Cumulative capacity (mAh $cm^{-2}$) |
|---|---|---|---|---|---|
| $MgCl_2$+$AlCl_3$+ $Mg(TFSI)_2$/THF[23] | 0.2 | 0.05 | ~100 | 90 | 9 |
| OMBB/DME[24] | 0.1 | 0.05 | ~40 | 700 | 35 |
| $Mg(HMDS)_2$ +$AlCl_3$/DG[25] | 0.5 | 0.125 | ~150 | 130 | 32.5 |
| MgBhfip/DME[26] | 0.1 | 0.05 | ~100 | 1200 | 60 |
| LBhfip/DME[13] | 1 | 0.5 | ~220 | 2000 | 1000 |
| MgFPA/THF[27] | 1 | 0.5 | ~140 | 1200 | 600 |
| $Mg(CB_{11}H_{12})_2$ /DME-TG[28] | 20 | 3 | ~300 | ~83 | ~834 |
| $MgCl_2$+$AlCl_3$+ LiCl/THF-IL[29] | 0.5 | 0.5 | ~140 | 500 | 125 |
| $Mg(OTf)_2$+$MgCl_2$+ $AlCl_3$/DME[30] | 0.05 | 0.05 | ~200 | 200 | 5 |
| $Mg(HMDS)_2$+TBA $BH_4$/DME[18] | 0.5 | 0.5 | ~250 | 2000 | 500 |
| $Mg(TFSI)_2$/DME -TMP[31] | 0.1 | 0.025 | ~500 | 300 | 15 |
| $Mg(TFSI)_2$+$MgCl_2$ +rPDI/DME[32] | 1.0 | 1.0 | ~250 | 300 | 150 |
| $Mg(OTf)_2$ +$MgCl_2$/DME[1] | 0.5 | 1 | ~200 | 500 | 125 |
| $Mg(OTf)_2$+TBAC/ DME[15] | 0.5 | 0.5 | ~290 | 600 | 300 |
| $Mg(pftb)_2$ +$MgCl_2$/THF[19] | 2 | 0.5 | ~160 | 1550 | 1550 |
| MLCC-1T1B[20] | 15 | 2 | ~500 | 250 | ~1874 |
| | 20 | 3 | ~600 | 170 | ~1698 |
| $Mg(TFSI)_2$+$MgCl_2$/ DME+THF[22] | 1 | 1 | ~150 | 700 | 350 |
| **$Mg(OTf)_2$ + CP/DME (this work)** | **1** | **1** | **~110** | **1700** | **850** |
| | **5** | **5** | **~420** | **420** | **1050** |
| | **25** | **1** | **~900** | **220** | **2750** |
| | **20** | **2** | **~740** | **160** | **1600** |
| | **20** | **3** | **~730** | **130** | **1300** |

**References:**


1 D.-T. Nguyen, A. Y. S. Eng, M.-F. Ng, V. Kumar, Z. Sofer, A. D. Handoko, G. S. Subramanian and Z. W. Seh, *Cell Rep. Phy. Sci.*, 2020, **1**, 100265.

2 C. Lee, W. Yang and R. G. Parr, *Phys. Rev. B*, 1988, **37**, 785-789.

3 S. Grimme, S. Ehrlich and L. Goerigk, *J. Comput. Chem.*, 2011, **32**, 1456-1465.

4 T. H. Dunning, *J. Chem. Phys.*, 1989, **90**, 1007-1023.

5 M. J. Frisch, *et al. Gaussian 16, Wallingford, CT* Rev. A.03 **2016**.

6 T. Lu and F. Chen, *J. Comput. Chem.*, 2012, **33**, 580-592.

7 J. P. Perdew, K. Burke and M. Ernzerhof, *Phys. Rev. Lett.*, 1996, **77**, 3865-3868.

8 G. Kresse and J. Furthmüller, *Phys. Rev. B*, 1996, **54**, 11169-11186.

9 P. E. Blöchl, *Phys. Rev. B*, 1994, **50**, 17953-17979.

10 S. Grimme, J. Antony, S. Ehrlich and H. Krieg, *J. Chem. Phys.*, 2010, **132**, 154104.

11 X. Fan, L. Chen, X. Ji, T. Deng, S. Hou, J. Chen, J. Zheng, F. Wang, J. Jiang, K. Xu and C. Wang, *Chem*, 2018, **4**, 174-185.

12 O. Mizrahi, N. Amir, E. Pollak, O. Chusid, V. Marks, H. Gottlieb, L. Larush, E. Zinigrad and D. Aurbach, *J. Electrochem. Soc.*, 2008, **155**, A103.

13 K. Tang, A. Du, S. Dong, Z. Cui, X. Liu, C. Lu, J. Zhao, X. Zhou and G. Cui, *Adv. Mater.*, 2020, **32**, e1904987.

14 W. Ren, D. Wu, Y. NuLi, D. Zhang, Y. Yang, Y. Wang, J. Yang and J. Wang, *ACS Energy Lett.*, 2021, **6**, 3212-3220.

15 D.-T. Nguyen, A. Y. S. Eng, R. Horia, Z. Sofer, A. D. Handoko, M.-F. Ng and Z. W. Seh, *Energy Storage Mater.*, 2022, **45**, 1120-1132.

16 G. Yang, Y. Li, C. Zhang, J. Wang, Y. Bai, C. Y. J. Lim, M.-F. Ng, Z. Chang, S. Kumar, Z. Sofer, W. Liu and Z. W. Seh, *Nano Lett.*, 2022, **22**, 9138-9146.

17 D. Chinnadurai, W. Y. Lieu, S. Kumar, G. Yang, Y. Li and Z. W. Seh, *Nano Lett.*, 2023, **23**, 1564-1572.

18 R. Horia, D.-T. Nguyen, A. Y. S. Eng and Z. W. Seh, *Nano Lett.*, 2021, **21**, 8220-8228.

19 J. Xiao, X. Zhang, H. Fan, Y. Zhao, Y. Su, H. Liu, X. Li, Y. Su, H. Yuan, T. Pan, Q. Lin, L. Pan and Y. Zhang, *Adv. Mater.*, 2022, **34**, e2203783.

20 J. Xiao, X. Zhang, H. Fan, Q. Lin, L. Pan, H. Liu, Y. Su, X. Li, Y. Su, S. Ren, Y. Lin and Y. Zhang, *Adv. Energy Mater.*, 2022, **12**, 2202602.

21 S. Hou, X. Ji, K. Gaskell, P.-f. Wang, L. Wang, J. Xu, R. Sun, O. Borodin and C. Wang, *Science*, 2021, **374**, 172-178.

22 Y. Sun, Y. Wang, L. Jiang, D. Dong, W. Wang, J. Fan and Y.-C. Lu, *Energy Environ. Sci.*, 2023, **16**, 265-274.

23 Y. He, Q. Li, L. Yang, C. Yang and D. Xu, *Angew. Chem. Int. Ed.*, 2019, **58**, 7615-7619.

24 A. Du, Z. Zhang, H. Qu, Z. Cui, L. Qiao, L. Wang, J. Chai, T. Lu, S. Dong, T. Dong, H. Xu, X. Zhou and G. Cui, *Energy Environ. Sci.*, 2017, **10**, 2616-2625.

25 Y. Xu, W. Li, G. Zhou, Z. Pan and Y. Zhang, *Energy Storage Mater.*, 2018, **14**, 253-257.

26 Z. Zhao-Karger, R. Liu, W. Dai, Z. Li, T. Diemant, B. P. Vinayan, C. Bonatto Minella, X. Yu, A. Manthiram, R. J. Behm, M. Ruben and M. Fichtner, *ACS Energy Lett.*, 2018, **3**, 2005-2013.

27 K. Tang, A. Du, X. Du, S. Dong, C. Lu, Z. Cui, L. Li, G. Ding, F. Chen, X. Zhou and G. Cui, *Small*, 2020, **16**, 2005424.

28 H. Dong, O. Tutusaus, Y. Liang, Y. Zhang, Z. Lebens-Higgins, W. Yang, R. Mohtadi and Y. Yao, *Nat. Energy*, 2020, **5**, 1043-1050.

29 H. Fan, Z. Zheng, L. Zhao, W. Li, J. Wang, M. Dai, Y. Zhao, J. Xiao, G. Wang, X. Ding, H. Xiao, J. Li, Y. Wu and Y. Zhang, *Adv. Funct. Mater.*, 2020, **30**, 1909370.

30 D. Huang, S. Tan, M. Li, D. Wang, C. Han, Q. An and L. Mai, *ACS Appl. Mater. Interfaces*, 2020, **12**, 17474-17480.

31 W. Zhao, Z. Pan, Y. Zhang, Y. Liu, H. Dou, Y. Shi, Z. Zuo, B. Zhang, J. Chen, X. Zhao and X. Yang, *Angew. Chem. Int. Ed.*, 2022, **61**, e202205187.

32 Y. Sun, Q. Zou, W. Wang and Y.-C. Lu, *ACS Energy Lett.*, 2021, **6**, 3607-3613.